Seismogenic structures and active creep in the Granada Basin (S-Spain)

Daniel Stich [a,b,*], Jose Morales [a,b], José Ángel López-Comino [a,b], Carlos Araque-Pérez [a], José Miguel Azañón [c], Miguel Ángel Dengra [a], Mario Ruiz [d], Moisés Weber [e]

[a] Instituto Andaluz de Geofísica, Universidad de Granada, Granada, Spain
[b] Departamento de Física Teórica y del Cosmos, Universidad de Granada, Granada, Spain
[c] Departamento de Geodinámica, Universidad de Granada, Granada, Spain
[d] IFMIF-DONES España, Granada, Spain
[e] Centro de Investigaciones Energéticas, Medioambientales y Tecnológicas (CIEMAT), Madrid, Spain

ARTICLE INFO

ABSTRACT

The Granada Basin is a slowly deforming intramountain basin in the Betic Cordillera (S-Spain). Despite historical and paleoseismological evidence for M6 earthquakes, instrumental seismicity lacks large events and the seismotectonic model must be built from small earthquakes (M < 5). Here, we reanalyze 35 years of data from the Granada Basin short period network, and further seismic stations with shorter operating time, to identify seismogenic structures and understand their relationships. We sort events with similar waveforms into multiplet clusters and perform relative location to image active fault patches. Cluster orientations are used as a priori constraint for inverting focal mechanisms from composite cluster polarity measurements. We further estimate moment tensor solutions from full waveform inversion using local and regional broadband stations. We can identify four groups of structures at different positions in the basin: 1) in the northeast sector, we observe shallow, NW-SE striking, high-angle normal faulting, often related with known fault structures; 2) the southern sector shows high-angle normal faulting on unmapped, ~E-W striking structures at mid-crustal depths; 3) between both groups, we image sub-horizontal fault patches, associated with the basal detachment beneath the basin, showing SSW transport direction; 4) at the western limit of the basin, we find ~N-S trending, left-lateral strike-slip faults. Groups 2 and 3 are characterized by clusters with overall constant event production rate, indicating ongoing and largely aseismic creep of the basal detachment over the last 35 years. Seismological evidence suggests a locking depth of ~10 km and a brittle-ductile transition near 15 km, according to the depth range of clusters in groups 2 and 3.

1. Introduction

Seismogenic faults are those structures that generate earthquakes, owing to their role in present-day strain localization, their strength and their frictional properties. Due to a lack of knowledge about fault parameters, seismogenic faults are usually identified through the available geological, historical or instrumental records of earthquake activity in the past. The recognition of seismogenic structures has received considerable attention, since it is essential for understanding seismotectonics and assessing seismic hazard. Potential sources of earthquakes have been compiled in databases of active structures, mostly based on the criteria of fault activity during the Quaternary (e.g., Basili et al., 2013, 2022; Mohadjer et al., 2016; Danciu et al., 2018; Styron et al., 2020; Styron and Pagani, 2020). Generally, a high degree of

correspondence is assumed between the sets of Quaternary faults (2.59 Ma) and seismogenic structures, although actually only for a subset of structures there is evidence for specific fault slip events at seismogenic speed. On the other hand, small and moderate magnitude earthquakes can occur also on unknown faults, without surface expression nor previous knowledge from subsurface imaging (e.g., Stich et al., 2005; Biggs et al., 2006). A comprehensive compilation of the relevant regional structures is particularly challenging in settings of slow strain accumulation and long recurrence intervals for significant earthquakes. In this study, we use instrumentally recorded seismicity to identify seismogenic structures and establish a seismotectonic model of the Granada Basin (Southern Spain).

The Granada Basin is a Neogene-Quaternary intramountain Basin within the Betic range (Fig. 1), located at the hanging wall of a low-angle

extensional system (Morales et al., 1997; Galindo-Zaldívar et al., 1999; Rodríguez-Fernández et al., 2011; Azañón et al., 2012; Martin-Rojas et al., 2023). In view of the obliquely convergent plate motion between Eurasia and Nubia (Kreemer et al., 2014), ongoing extension in the Betic range may be attributed to sublithospheric processes. The Betic-Alboran region is located on top of the Gibraltar slab (Bezada et al., 2013; Fichtner and Villaseñor, 2015) and extension may be driven by slab retreat (Lonergan and White, 1997; Faccenna et al., 2004; Gutscher et al., 2012), partial detachment and tearing of the slab (Mancilla et al., 2015; Heit et al., 2017) and southwest directed drag from the relative motion of the hanging slab through the surrounding mantle (Spakman et al., 2018; Capella et al., 2020). The extensional regime is clearly represented in available seismic moment tensors and the GNSS velocity field. Moment tensor estimates for small to moderate magnitude events at the Granada Basin indicate mostly normal faulting style and an ENE-WSW direction of extension, parallel to the trend of the Betics (Stich et al., 2006, 2020; Martín et al., 2015). Extension along the entire Betic range has been quantified as about 2 mm/year to 2.5 mm/year (e.g., Stich et al., 2006; Serpelloni et al., 2007, 2022), of which the most important extensional strain can be located in the central sector of the mountain range (Mancilla et al., 2013; Palano et al., 2015; Garate et al., 2015). Recent estimates suggest that about 1.3 mm/year of Betic extension is currently occurring at the Granada Basin (Martin-Rojas et al., 2023).

In accordance with the tectonic regime, normal faults are the predominant neotectonic structures that can be observed in seismic reflection lines and surface geology of the Granada Basin, some of them with prominent geomorphological expressions and well-preserved fault scarps (Morales et al., 1990; Sanz de Galdeano et al., 2003, 2012; Galindo-Zaldívar et al., 2003; Rodríguez-Fernández and Sanz de

Galdeano, 2006; Pérez-Peña et al., 2015; Madarieta-Txurruka et al., 2021). The Iberian database of fault source models (García-Mayordomo et al., 2012; García-Mayordomo and Martín-Banda, 2022) assigns fault activity during the Upper Pleistocene to Holocene period (< 125.000 years) to four of these structures: the Atarfe, Pinos Puente, Padul-Niguelas and Ventas de Zafarraya faults (Fig. 2). Among them, only the Ventas de Zafarraya fault has been associated unambiguously with a specific major earthquake, showing surface rupture in the 1884 Andalusian, or Christmas earthquake (M_W 6.5–6.7, Reicherter et al., 2003, Grützner et al., 2013). Other faults are located in areas of low rate of instrumental seismicity (e.g. Padul-Niguelas fault) or high rate of instrumental seismicity (e.g. Atarfe and Pinos Puente faults, Fig. 2), but have unclear relationship to specific seismic events or series (e.g. Lozano et al., 2022; Madarieta-Txurruka et al., 2022). Here, we reanalyze 35 years of instrumental seismicity of the Granada Basin since the installation of local seismic stations in the 1980s, performing earthquake cluster detection, relative location, cluster focal mechanism inversion and regional moment tensor inversion. We attempt collecting evidence for the seismogenic or aseismic behavior of recognized fault structures, as well as characterizing the position, orientation and cinematics of unmapped tectonic structures that have produced instrumental seismicity.

2. Seismicity and seismic data

The Granada Basin area is characterized by the occurrence of frequent small and moderate magnitude earthquakes, as well as rare strong events (Mezcua and Martínez Solares, 1983; Vidal, 1986). In particular, two mayor earthquakes in 1431 and 1884 stand out from the historical records. In 1431, earthquakes were reported for April 24th
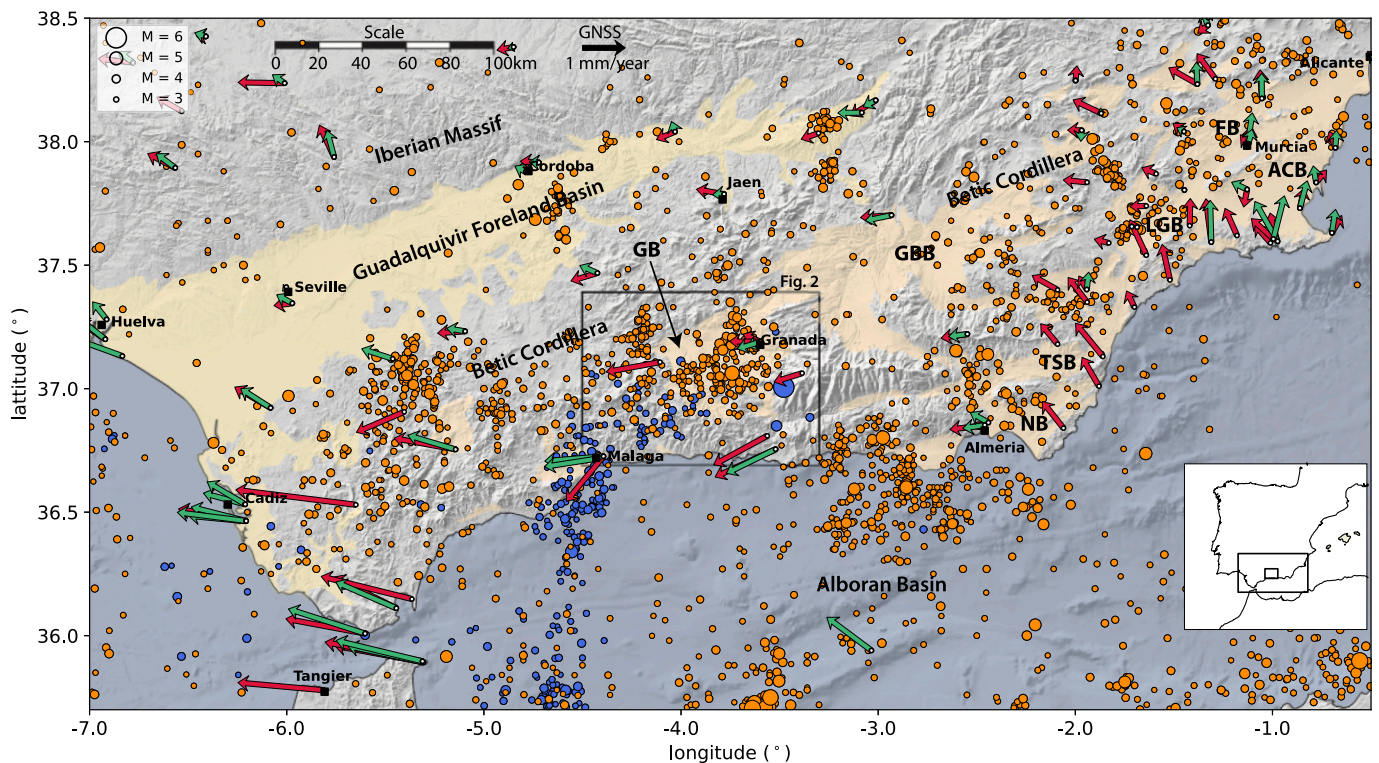
Fig. 1. Shaded relief map of the Betic Cordillera in S-Spain, including location of Neogene-Quaternary foreland basins (light yellow) and intramountain basins (dark yellow; GB: Granada Basin, GBB: Guadiz-Baza Basin, FB: Fortuna Basin, ACB: Alicante-Cartagena Basin, LGB: Lorca-Guadalentin Basin, TSB: Tabernas-Sorbas Basin, NB: Níjar Basin), seismicity since 1980 (Reviewed ISC Bulletin, International Seismological Centre, 2023) with magnitudes ≥3, and horizontal velocities at permanent GNSS stations with respect to stable Eurasia (red arrows from Palano et al., 2015, green arrows from Serpelloni et al., 2022 in ITRF2008 reference frame). Three anomalous GNSS vectors in the Guadalentin Basin, close to the 2011 Lorca earthquake (López-Comino et al., 2012) and to groundwater overexploitation, were removed. The study area (Fig. 2 and following) is marked by the black box. Orange circles denote earthquakes shallower than 50 km and blue circles denote deeper events. (For interpretation of the references to colour in this figure legend, the reader is referred to the web version of this article.)
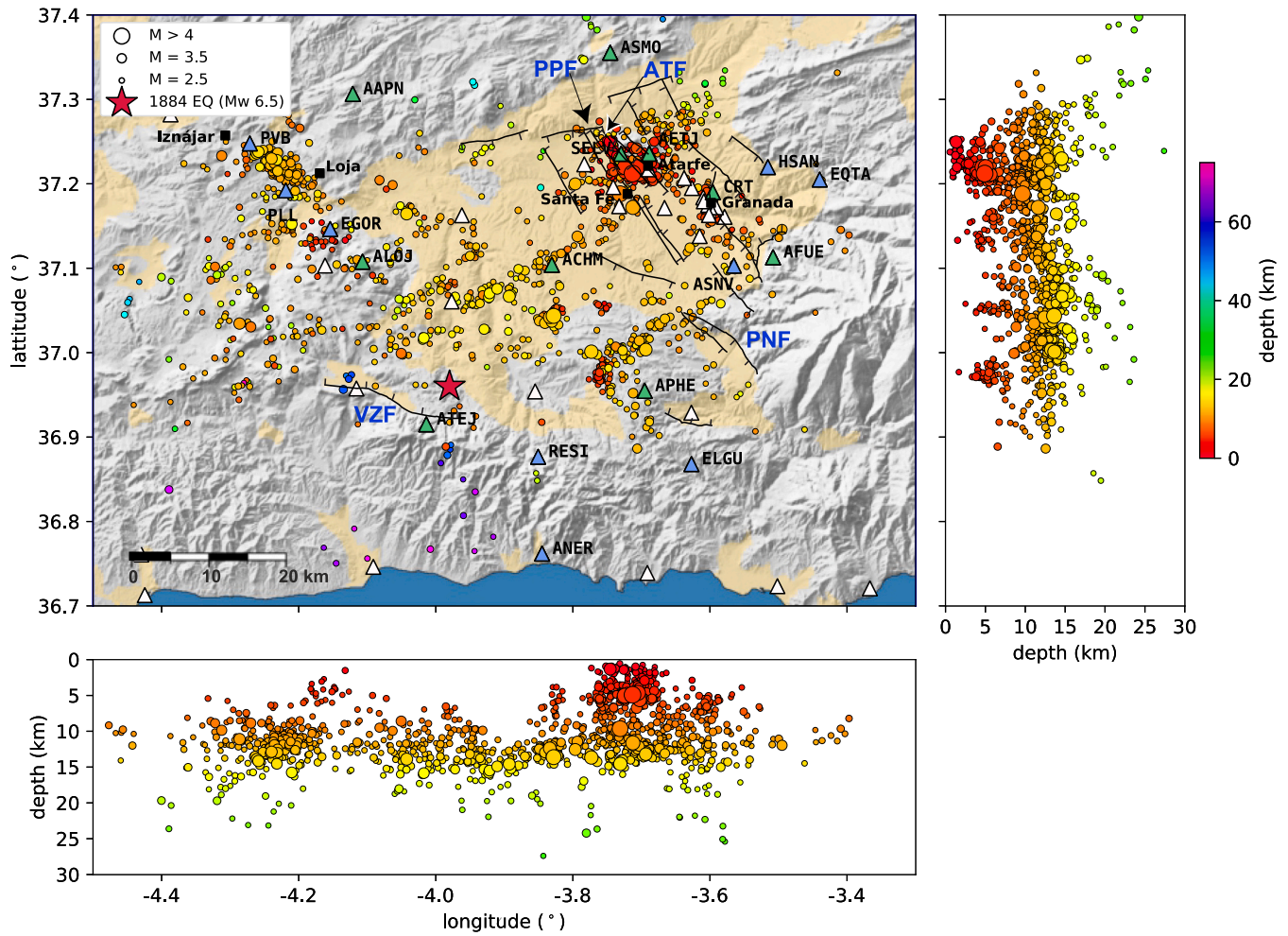
Fig. 2. Shaded relief map of the Granada Basin, with Neogene-Quaternary sediments in yellow (Instituto Geográfico Nacional, 2020). Seismicity shows events with magnitudes ≥2.5 since the installation of the local network in 1988 from the double difference hypocenter catalogue by Instituto Andaluz de Geofísica (IAG; depths colour coded). Seismic stations operated by IAG and Instituto Geográfico Nacional (IGN) are represented as triangles (green filling: stations used for cluster detection; blue filling: additional stations used for relative location; white filling: other stations, mainly recently deployed accelerometers). Faults from QAFI database (García-Mayordomo and Martín-Banda, 2022; catalogued Quaternary faults VZF: Ventas de Zafarraya Fault, PNF: Padul-Nigüelas Fault, ATF: Atarfe Fault, PPF: Pinos Puente Fault). (For interpretation of the references to colour in this figure legend, the reader is referred to the web version of this article.)

and beginning of July, most likely between July 8th and 10th according to a cross-validation with accounts of the battle of La Higueruela (Espinar-Moreno, 2022). The July earthquake apparently reached macroseismic intensity of IX in the city of Granada, and thus a magnitude probably above 6 (Vidal, 2011). On December 25th 1884, an intensity IX-X earthquake occurred at the south-western edge of the basin, known as the Andalusian Earthquake, claiming nearly 1000 lives in a sparsely populated area. The earthquake ruptured about 16 km of the Ventas de Zafarraya fault producing maximum surface displacement of 1.5 m, corresponding to an estimated moment magnitude M_W 6.5–6.7 (Reicherter et al., 2003). About another ten historic events at the Granada Basin over the last 500 years seem to have reached intensities of VII or VIII (Mezcua and Martínez Solares, 1983, Vidal, 1986), which may correspond to magnitude 5 events. Seismicity since the availability of local seismic recordings in the 1980s is lacking large magnitude events, so the characteristics of the earthquake distribution have to be inferred from small events. The largest event recorded on digital stations occurred on June 24th 1984, with moment magnitude of 5.0 (Morales et al., 1996; Stich et al., 2003).

The detection and location of small events and the compilation of a local earthquake catalogue has been carried out at the Instituto Andaluz de Geofísica (IAG) of Granada University since the start of operation of

the permanent seismic network in late 1987 (Alguacil et al., 1990). The original network consisted of seven vertical component, Mark L4C (1 Hz) stations and one three-component short-period station (ACRT, Fig. 2). Signals were radio transmitted to the IAG central recording site, and event data were stored digitally at 100 samples per second. All channels use a common time reference, which makes early locations already robust against possible errors in synchronization to the DCF77 clock signal (Alguacil, 1986). This short-period network is still in operation today, providing the backbone of this study with 35 + years of earthquake recordings by now. From the late 1990s on, the IAG put into operation an Andalusian seismic broadband network, with the installation of stations SELV in 1997 and ANER in 1998. Since then, further three-component broadband sensors at local and regional distances have been installed by IAG and the Instituto Geográfico Nacional (IGN), including EQTA (2005), HSAN (2007), ELGU (2011), EGOR (2011) and AETJ (2013) inside or near the Granada Basin. Additionally, a number of stations with shorter operational life contribute to the data inventory, including several temporary installations and the recently upgraded accelerometer network, of which 25 stations (operated by IAG or IGN) are located in or near the basin.

The instrumental catalogue of local earthquakes shows the spatial and temporal characteristics of seismicity and the active sectors within

the basin over the last 35 years (Fig. 2). Several main features emerge from double difference location (Waldhauser and Ellsworth, 2000; Waldhauser, 2001), based on the IAG catalogue phase readings and an average 1D wave speed and density model for the Betic Cordillera lithosphere (Stich et al., 2003). Background seismicity at the Granada Basin shows a wide distribution, including important spatio-temporal concentrations of events in form of seismic swarms, without clearly defined mainshock. The northeastern part of the basin is currently the most active sector, including the 2021 seismic series near Atarfe and Santa Fe (Madarieta-Txurruka et al., 2021, 2022; Lozano et al., 2022). Other relevant seismic series include the Agrón swarm of 1988–89 (Saccorotti et al., 2002) and the Iznajar-Loja swarm in 1998 (Carmona et al., 2009). Earthquake swarms represent a complex sequence of energy release and may be promoted by high fluid pressures, local heterogeneity or ongoing slow slip events (Vidale and Shearer, 2006), although so far, no conclusion had been reached on the factors that control swarm activity in the Granada Basin. In contrast to swarms, the largest instrumentally recorded earthquakes so far are associated to sequences with a single mainshock and low aftershock activity, such as the June 24th 1984, $M_W = 5.0$ event (Morales et al., 1996) and the August 12th 2021, $M_W = 4.5$ event (Lozano et al., 2022).

Seismic activity in the Central Betics is covering a large depth range from the shallow crust to the base of the mantle transition zone. Subcrustal earthquakes are concentrated in an area southwest of the Granada Basin, reaching depths of ~100 km (Morales et al., 1997; Santos-Bueno et al., 2019). Isolated, very deep focus earthquakes have been detected beneath the southeastern sector of the Basin, with depths of about 650 km and significant magnitudes ($M_W = 7.8$ in 1954 and $M_W = 6.3$ in 2010; Chung and Kanamori, 1976, Buforn et al., 2011, Mancilla et al., 2012, Bezada and Humphreys, 2012). Crustal seismicity, which is the subject of this study, is occurring mainly at shallow depths (0–10 km) in the northeastern sector of the Basin and concentrating in the middle crust (10 km to 15 km depth) in the central, southern and western parts of the study area (Fig. 2). The shallow events in the northeast have been associated with high angle normal faults in this sector (Madarieta-Txurruka et al., 2022; Lozano et al., 2022). From the surface rupture of the 1884, M_W 6.5–6.7 earthquake, we know that shallow normal faulting is also active at the opposite border of the basin, although no significant seismic activity has been detected in this sector since the installation of the local network. The seismicity in the middle crust appears highly localized in a narrow depth interval, getting gradually deeper towards the southwest (Fig. 2). Mid-crustal seismicity has been interpreted as the signature of a subhorizontal shear zone representing an active low-angle normal fault, or basal detachment, beneath the basin (Morales et al., 1997; Galindo-Zaldívar et al., 1999; Madarieta-Txurruka et al., 2021; Martin-Rojas et al., 2023).

3. Moment tensor inversion

The first order seismic moment tensor is a general description of seismic point sources, containing information on the source mechanism and the scalar seismic moment (Silver and Jordan, 1982) or associated moment magnitude M_W (Hanks and Kanamori, 1979). We use time-domain moment tensor inversion from complete three-component, intermediate period waveforms recorded at regional distances (IAG moment tensor catalogue; Stich et al., 2003). Green's functions are computed from a reflection-matrix method (Randall, 1994) for a plane layered Earth model that represent the average structure of the Betic lithosphere (model b in Stich et al., 2003). Waveforms are bandpass filtered between 0.02 Hz and 0.05 Hz for earthquakes with magnitudes $\gtrsim 4$, and between 0.028 Hz and 0.065 Hz for smaller events. This Earth model and frequency range have been shown to allow adequate modelling for earthquakes from the Betics at most regional seismic stations in southern Spain (Stich et al., 2010). IAG moment tensors published up to 2014 include 14 solutions for the Granada Basin and nearby areas (Martín et al., 2015). The earliest solutions date from the

late 1990s, when regional broadband recordings became available, with exception of the 1984, $M_W = 5.0$ earthquake (Stich et al., 2003) that has been analysed from recordings at three temporary broadband stations from the NARS-Europe (Network of Autonomously Recording Seismographs) deployment.

Here we present an update of the catalogue, examining earthquakes with reported magnitudes ≥3.2 in the IAG hypocenter catalogue till end of 2022. We combine linear least squares moment tensor inversion with a grid search over centroid depths, to account for the depth sensitivity of the Green's functions and to obtain an independent estimate of this parameter. The grid spacing of the trial centroid depths is 1 km through the upper crust. We assume deviatoric moment tensors and report sources through their double-couple tensors and residual compensated linear vector dipoles (clvd), quantifying the formal deviation from shear faulting. A careful selection of waveforms and preprocessing is carried out, including a manual tuning of weighting of the waveforms for inversion, in order to improve the overall quality of waveform matches and obtain stable solutions. We illustrate typical recording geometries, waveform matching and depth resolution for events from the 2021 Santa Fe-Atarfe earthquake series and from the southern sector of the basin (Fig. 3). Event 20210126 A represents the first of a succession of three widely felt earthquakes within 20 min, showing nearly pure normal faulting, in consonance with other moment tensor solutions for this series (Table 1). Source depth is shallow, with the formally best solution obtained at 5 km depth, showing a nearly pure double couple tensor (2% clvd). Event 20,170,518 shows smaller moment magnitude of 3.5 and significantly larger noise level in the intermediate period seismograms (Fig. 3b). Still, part of the signal emerges from the noise and we can fit most vertical components and several of the horizontal seismograms. A proper adjustment of weights is challenging in this case, and the large clvd component (23%) presumably reflects contamination of the moment tensor by noise. Compared to the 2021 earthquake, this event shows larger centroid depth of 13 km and a more *E*-W direction of the nodal planes.

Altogether, we were able to obtain 18 new moment tensor estimates (Table 1). The solutions corroborate the main tendencies observed in previous studies, in particular the dominant role of normal faulting in the basin (Stich et al., 2006). A majority of normal faulting mechanisms show nodal planes with ~NW-SE orientation, which are mainly located towards the northern and eastern limits of the basin, including the solutions for the 2021 Santa Fe-Atarfe series (Fig. 4). Centroid depths in this sector are mostly shallow, from 3 km to 7 km, suggesting a relationship of the events with the high-angle normal faults exposed at the surface (Sanz de Galdeano et al., 2003; Madarieta-Txurruka et al., 2022; Lozano et al., 2022). In the central-southern part of the basin we observe notably different normal faulting mechanisms with nodal plane orientation closer to E-W and deeper centroids, close to the presumed detachment horizon beneath the basin. At the western termination of the basin, we can observe mechanisms with different faulting style and orientation, including a NE-SW striking normal faulting solution (20220929), oblique faulting (20151010) and strike-slip solutions with NE-SW extensional axes. The largest event of this update (20,210,812, M_W 4.5) unfortunately coincides with the coda of a magnitude 8.1 earthquake at the South Sandwich Islands, which is significantly contaminating the intermediate-period waveforms (compare Lozano et al., 2022). We achieve a stable outcome for magnitude and faulting style, but the depth and orientation of the mechanism are largely undefined. The updated moment tensor inventory provides dense coverage for a large part of the study area, and will be compared with the results of earthquake cluster analysis down below.

4. Cluster detection and relative location

The common occurrence of seismic series and swarms in the Granada Basin, showing strong spatial clustering of events (Saccorotti et al., 2002; Carmona et al., 2009; Madarieta-Txurruka et al., 2022; Lozano
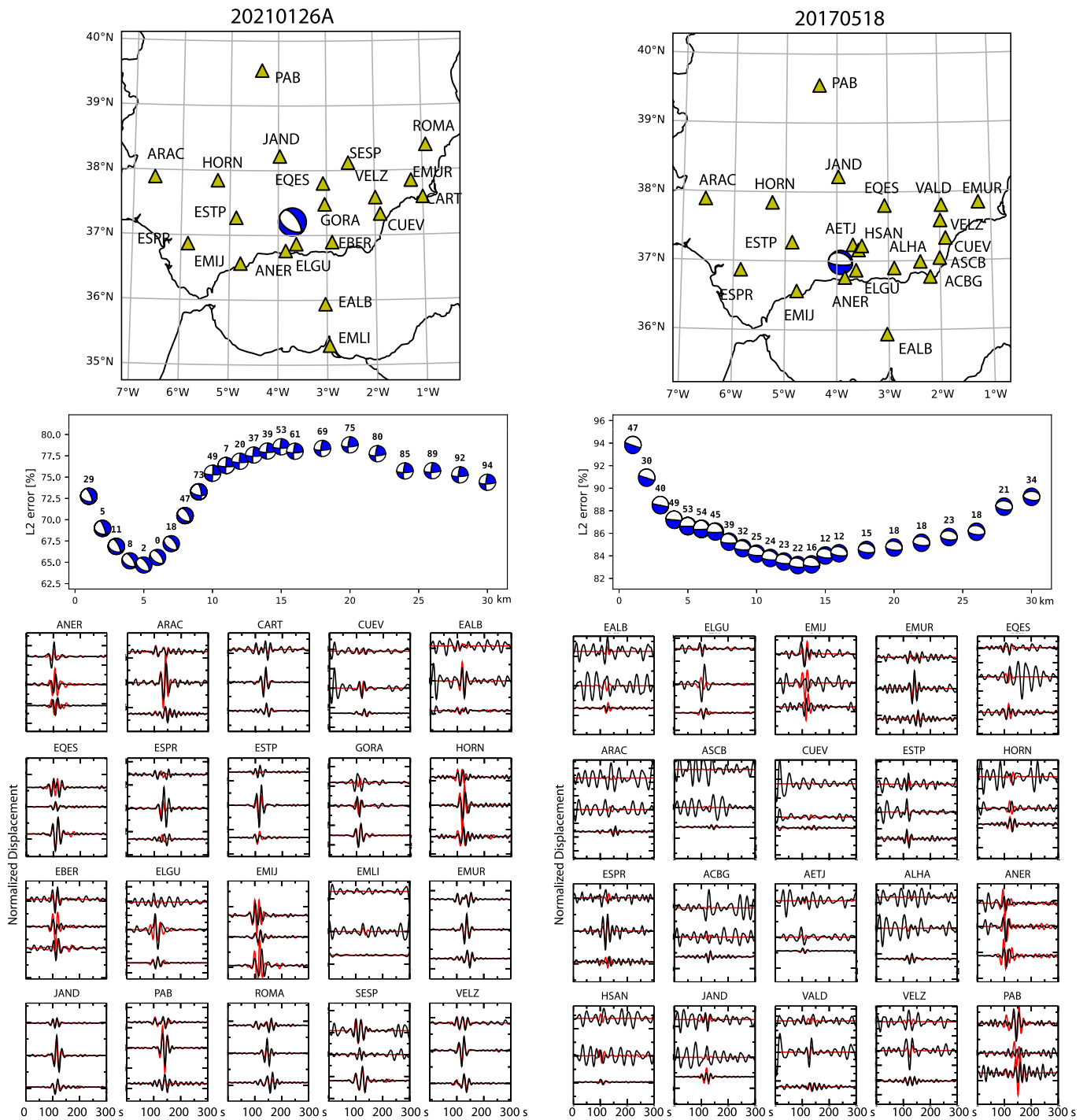
Fig. 3. Examples of moment tensor inversion for events 20210126 A (left) and 20,170,518 (right). Maps show used stations as triangles. Misfit versus depth curves show also the variation of mechanism and clvd component (numbers above beachballs). Waveform matches show normalized observed (black) and predicted (red) waveforms on radial, transverse and vertical components (from top to bottom, in each station panel). (For interpretation of the references to colour in this figure legend, the reader is referred to the web version of this article.)

et al., 2022), is a suitable scenario for performing relative hypocenter location. The relative location between near earthquakes can have greater accuracy than their absolute locations due to two reasons: Shortcomings of the Earth model affect at nearby events in a similar way, and the P- and S- wave arrivals times can be determined with higher internal consistency, using the waveform similarity between recordings from nearby events to provide a reference for the identification and alignment of phase arrivals. To map the orientation of seismogenic structures in the Granada Basin we perform cluster detection and location using the digital waveforms from the IAG local seismic network for the 35-year period from January 1988 to December 2022. This includes 7 vertical component stations and three-component CRT (Fig. 2). To mitigate the prevalence of vertical component sensors in the original short period network, we integrate into cluster detection the three-

Table 1
Moment tensor solutions for the Granada Basin area. The event ID is constructed from the date and an optional capital letter in order of occurrence. Time is given in UTC. Latitude and longitude (Lat, Lon) according to IAG catalogue; depth z is the formally best-fitting centroid depth from moment tensor inversion. Columns s1 to r2 denote the strike, dip and rake values for the two nodal planes, with strike counted clockwise from north and dip counted positive to the right. Column clvd denotes the formal non-double component in percent. Mechanisms before 2014 are published in Martín et al. (2015), and references therein.

| Event ID	Date [d/m/y]	Time [h:m:s]	Lat [°]	Lon [°]	z [km]	s1 [°]	d1 [°]	r1 [°]	s2 [°]	d2 [°]	r2 [°]	M_W	clvd [%]
19,840,624	24/06/1984	14:30:52	36.86	−3.76	6	166	27	−78	333	64	−96	5.0	18
19,961,228	28/12/1996	07:30:36	37.17	−3.71	12	200	30	−35	323	73	−115	3.9	15
19,970,224	24/02/1997	07:09:50	37.04	−3.83	16	120	4	−92	302	86	−89	4.3	3
19980413 A	13/04/1998	05:55:41	37.23	−4.23	14	77	73	−143	335	55	−19	3.6	27
19980413B	13/04/1998	13:50:52	37.23	−4.24	14	87	72	−150	346	61	−20	3.6	15
19,980,414	14/04/1998	02:13:03	37.24	−4.26	12	88	69	−145	344	58	−25	3.5	27
19,981,118	18/11/1998	23:18:10	37.00	−3.77	8	134	66	−62	263	35	−135	4.1	19
20,030,910	10/09/2003	20:22:47	37.14	−3.79	12	143	17	−55	289	76	−100	3.8	22
20,070,104	04/01/2007	23:32:32	37.21	−3.74	6	83	44	−121	303	53	−62	3.7	1
20,070,609	09/06/2007	07:15:16	37.06	−3.58	12	188	38	−55	327	59	−114	3.4	8
20,071,001	01/10/2007	00:39:56	37.07	−3.93	6	107	62	−120	338	40	−46	3.5	7
20,091,105	05/11/2009	05:39:55	37.07	−3.89	26	100	28	−83	273	62	−93	4.0	1
20,100,411	11/04/2010	22:08:06	37.00	−3.69	620	55	24	−44	188	73	−107	6.3	1
20,140,709	09/07/2014	18:36:23	36.89	−3.96	60	66	43	28	315	71	130	4.0	6
20,140,325	25/03/2014	00:20:10	36.95	−3.71	13	69	45	−106	271	47	−75	3.6	8
20,151,010	10/10/2015	05:05:29	37.11	−4.12	40	85	39	−172	349	85	−51	3.7	17
20,170,518	18/05/2017	10:07:55	37.06	−3.94	13	94	69	−99	297	23	−68	3.5	23
20,170,629	29/06/2017	22:32:37	37.10	−3.85	18	168	31	−56	309	65	−109	3.4	10
20,170,731	31/07/2017	23:16:55	37.00	−3.56	11	211	31	−33	330	74	−117	3.5	2
20,180,617	17/06/2018	07:47:34	37.14	−4.28	18	257	63	159	357	72	29	3.5	23
20,181,009	09/10/2018	07:41:53	37.25	−3.75	3	148	20	−100	339	70	−86	3.9	27
20,201,202	02/12/2020	23:09:09	37.22	−3.73	6	153	46	−74	310	46	−106	3.6	13
20,210,123	23/01/2021	11:15:24	37.22	−3.71	5	140	36	−95	326	54	−87	4.3	11
20210126 A	26/01/2021	21:36:33	37.21	−3.70	5	123	37	−109	326	55	−76	4.1	3
20210126B	26/01/2021	21:44:18	37.21	−3.70	5	123	39	−103	320	53	−79	4.1	12
20210126C	26/01/2021	21:54:55	37.21	−3.71	5	114	40	−115	326	55	−71	4.4	5
20210128 A	28/01/2021	18:06:28	37.22	−3.72	7	126	41	−115	337	54	−70	3.6	4
20210128B	28/01/2021	18:49:49	37.22	−3.72	7	123	36	−111	329	57	−75	4.4	9
20210128C	28/01/2021	19:28:19	37.21	−3.70	7	108	40	−123	328	57	−65	3.6	25
20210128D	28/01/2021	21:29:04	37.22	−3.69	7	124	41	−112	332	53	−72	3.4	10
20,210,812	12/08/2021	21:25:12	37.19	−3.73	4	128	61	−67	267	36	−125	4.5	37
20,220,929	29/09/2022	09:14:45	37.16	−4.04	11	18	56	247	235	40	−60	3.5	27

component broadband station SELV and its successor AETJ (the station had to be reinstalled in 2013 due to a change of use at the original emplacement). This selection is motivated by the long operational record of these stations (since 1997) and the strategic location on a Mesozoic outcrop inside the basin, in close proximity to several seismic series.

The cluster assignment is based on waveform similarity, which is a necessary condition for measuring reliable relative arrival times (e.g. Maurer and Deichmann, 1995; Petersen et al., 2021). We apply pairwise cross correlations for events above a magnitude threshold of $Mc \geq 2.0$, which is usually associated with acceptable signal quality at several stations, keeping 9358 local events within the Granada Basin area (geographical limits of Fig. 2). Cross-correlation coefficients are measured in moving windows of 4 s duration, starting 1 s before the estimated P- and S-wave arrivals. Seismograms are bandpass filtered between 0.7 Hz and 2 Hz, which simplifies the waveforms significantly and which makes it feasible to detect relatively large clusters, through the evaluation of wavelengths on the order of kilometers. S-wave correlations are taken on horizontal seismograms for three-component stations, and on vertical components otherwise. To determine the average, or network-wide similarity for P- and S-waves for an event pair, negative cross-correlations, as well as the two smallest of the remaining values are discarded, which reduces bias from uncorrelated noise, especially for smaller events at distant stations. To avoid excess computational effort, cross-correlation is calculated only for event pairs with epicenter distances ≤10 km, as plausible candidates for high waveform similarity. This criterion reduces computing time by about one order of magnitude, leaving ~4 million event pairs within the selected distance threshold.

Network-wide cross correlations display a small fraction of values above 0.8 for S-waves and above 0.7 for P-waves, generally corresponding to event pairs with pronounced overall waveform similarity according to a visual assessment. Classification of similar events is performed with a density-based clustering algorithm (DBSCAN, Ester et al., 1996, as implemented in SKlearn1.2, SciKit), which has been established as a suitable technique for earthquake studies (Konstantaras et al., 2012; Cesca et al., 2014; Skoumal et al., 2019; Petersen et al., 2021). We define similar events via network-wide S-wave and P-wave correlation thresholds, and require a minimum number of five links to establish relationship with any cluster. The end members of a density-cluster are not required to comply with the correlation thresholds, which facilitates the unification of elongated clusters or the integration of mislocated event. The condition of multiple linkage stabilized the separation of clusters, although the assignment is still heavily dependent on the selected thresholds, which have effects on the completeness and separation of individual clusters. Instead of rigid threshold values, we employ an iterative cluster assignment, with stepwise increasing cross correlation thresholds from 0.80 (S-waves) and 0.70 (P-waves). In each step, clusters with high internal waveform similarity and compact distributions are extracted manually, while clusters that appear to merge elements from different earthquake groups are fed back into cluster analysis and processed with thresholds values increased by 0.02. After three iterations, a proper cluster separation for the remaining events was achieved using correlation thresholds of 0.84 and 0.74, respectively.

We identify 47 event clusters with at least 8 members (Fig. 5a), containing about 26% of the original catalogue events. The largest clusters correspond to the aforementioned Iznajar-Loja swarm of 1998 (cluster # 33 with 326 events) as well as to the Santa Fe-Atarfe seismic series of 2021 and previous, collocated activity since 1991 (# 14 with 563 events). The clusters show a wide distribution, with the main activity in the northeastern and southern sectors of the basin and in the area immediately to the west (Fig. 6). Several clusters coincide with
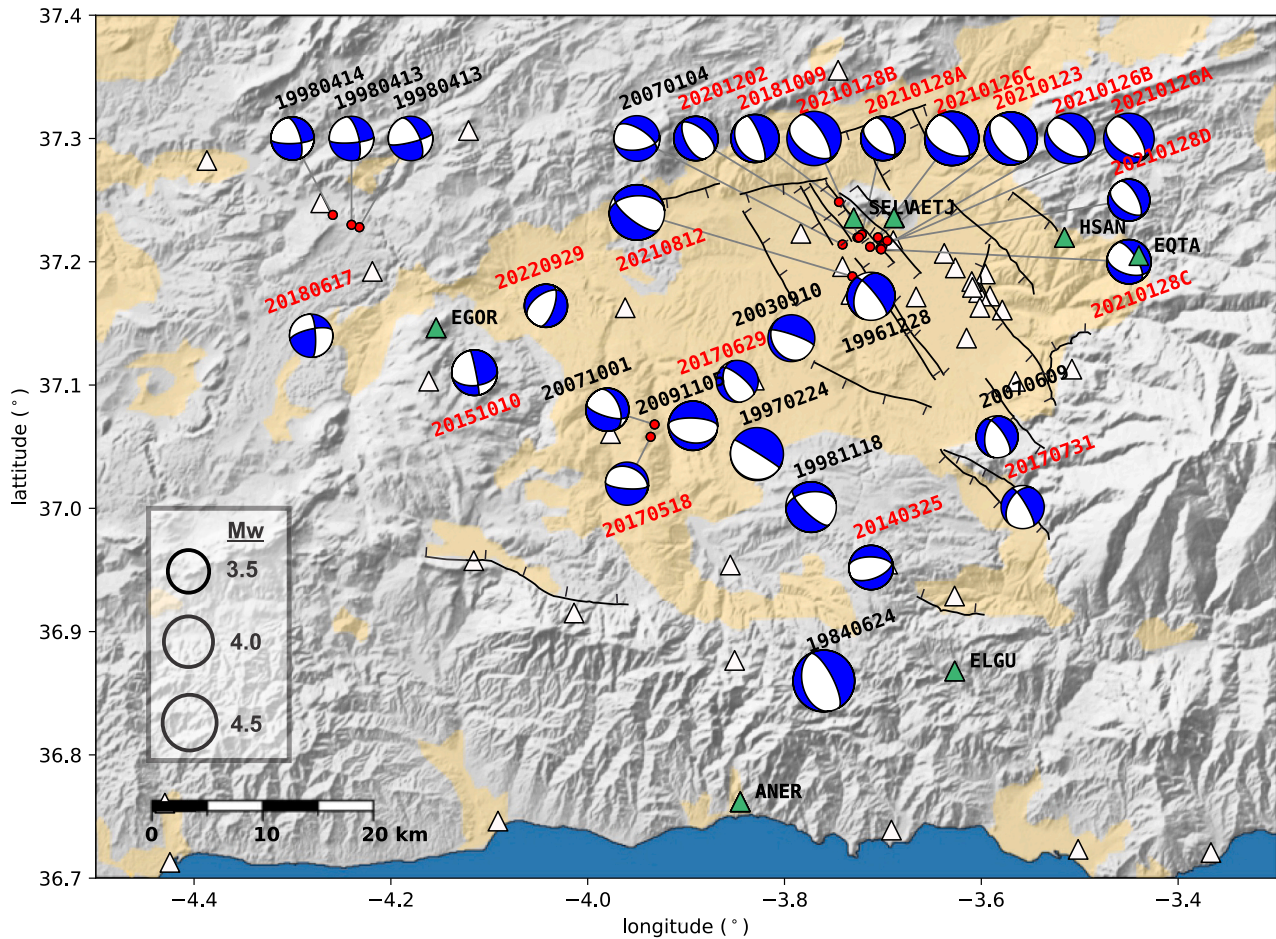
Fig. 4. Moment tensor mechanisms in lower hemisphere, equal area projection. Only the double couple component is shown. Relief, sediments and faults like in Fig. 2. Mechanisms are labeled with the identifier according to Table 1 (date plus optional letter), red labels for solutions from this study, black labels for solutions in Martín et al. (2015) and references therein. For the sake of visibility, some mechanisms have been shifted from their centroid locations (gray lines). Green triangles are local broadband stations used in inversion, for examples of regional broadband stations see Fig. 3. (For interpretation of the references to colour in this figure legend, the reader is referred to the web version of this article.)

quarry locations, and we check the nature of clustered events. Quarry blasts are an obvious example for repeated events with similar location and source process, and may be overrepresented in waveform-based cluster classification. While quarry blasts may be difficult to identify in routine database operations, they can be easily removed from clustered data, since they are characterized by a particular temporal pattern of events occurring solely during working hours and over a relevant time span (Fig. 5b). Accordingly, 18 clusters can be attributed to quarry activity, while 29 clusters correspond to natural earthquakes. The duration of natural earthquake clusters is highly variable, ranging from compact clusters such as # 44 and 47, showing a single burst of activity of less than one day, to clusters that were active during almost the entire observation period (# 01, 04, 05, 06, 9, 19, 21 and 17). We will address the different temporal characteristics of clusters in section 6.6.

Relative location within each cluster is achieved with a linear master event relocation scheme (Stich et al., 2001). We attempt to integrate recordings from additional broadband stations with shorter operational period (EQTA, ANER, EGOR, ELGU, HSAN) and temporary short-period instrumentation (PVB, PLL, ASNV, RESI; Fig. 2) when they are available for a majority of cluster events. The master event is selected according to the number of recording stations and the average correlation coefficient with all other events in the cluster. The relative arrival times are determined by two successive cross-correlations, the first one in larger windows (2 to 4 s for P-waves 3 to 5 for S-waves), to achieve a gross

alignment, and the second one in shorter, 1 to 2 s long windows for further finetuning on the first arrival. Window lengths are adapted for each cluster by trial and error. The successful alignment in a cluster is checked visually, and misaligned waveforms are excluded manually. The mean hypocenter location for the cluster is used as geometric reference to compute take-off angles. We use raytracing (module Cake in Pyrocko, Heimann et al., 2017), assuming the same Earth model as in moment tensor inversion.

Relocation results in km-scale hypocenter distributions, which is significantly smaller than the extend of cluster hypocenters in the routine catalogue (Figs. 6, 7). Most clusters show a pronounced planar component after relative location, confirming the presence of high-angle (e.g., # 06 and 20) and low-angle faults (e.g., # 9 and 21) in the basin (Fig. 7). The relocation of # 33 shows two separate fault segments, with the same strike direction and distance of 2 km, indicating the simultaneous activity of parallel faults during the 1998 Iznajar-Loja swarm and giving a glimpse of the seismotectonic fine structure in a highly fractured middle crust in this sector. For some clusters, we observe the migration of hypocenters along the structure. Cluster 10 first activates the southwestern patch, including the largest event of the series, and in the late stage of the series moves to the northeastern patch (Fig. 7). For # 33, we observe opposite trends for hypocenter migrations on either side, with upward and northward migration of seismicity on the western fault, and southward migration of seismicity on the eastern fault. For 23

a) Cluster assignment from P and S-waves

b) Origin time within clusters
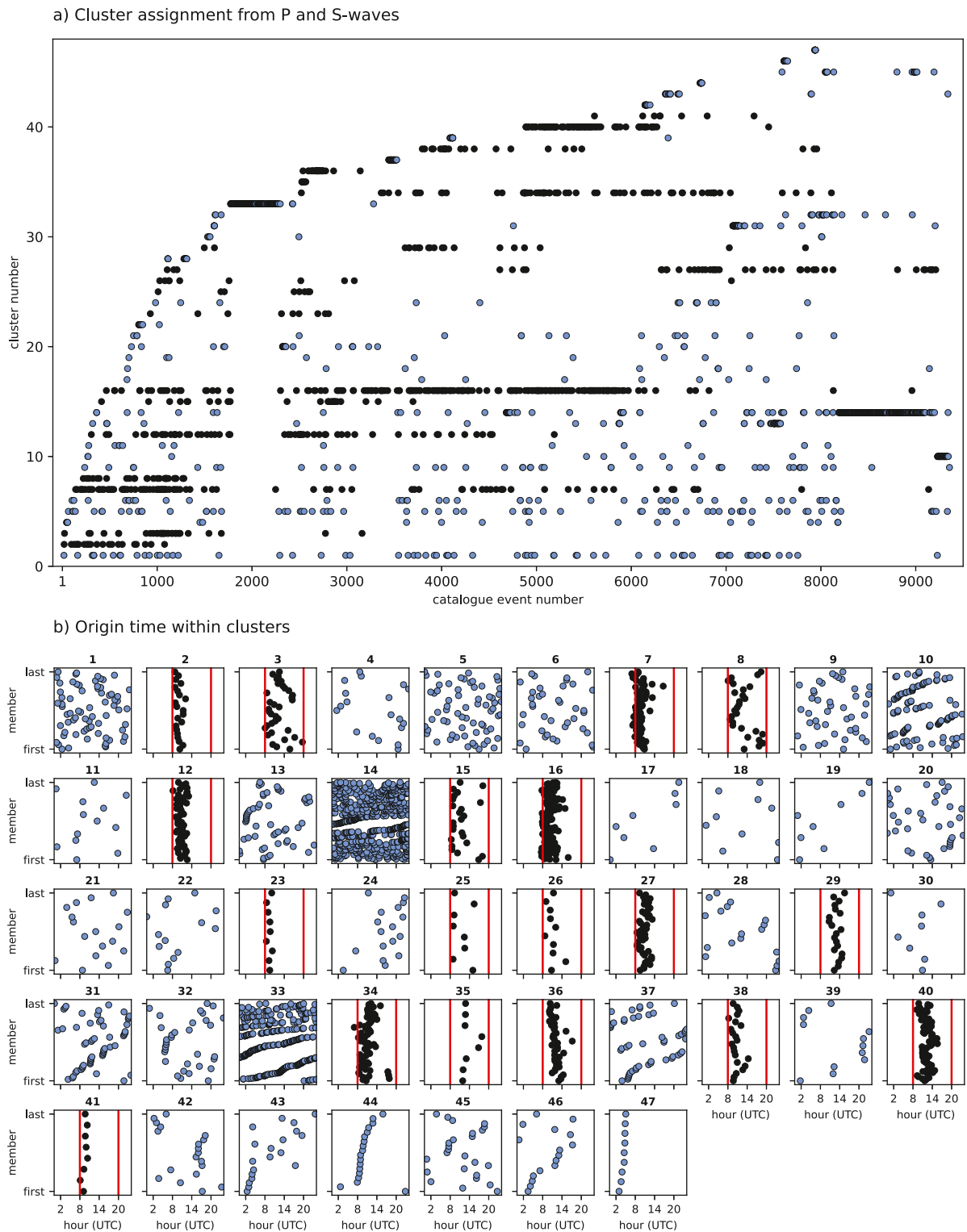
Fig. 5. a) Assignment of events (event number in temporal order) to detected clusters. The numbering of the clusters is done according to the temporal order of the first events. Black and blue colors denote clusters attributed to quarry activity and to natural earthquakes, respectively. b) Time (UTC) against order of events, with 8 UTC and 20 UTC marked by vertical lines, to identify clusters of presumed quarry blasts, which take place during working hours.

out of the 29 natural earthquake clusters, we estimate strike and dip values of the structures from principal component analysis (Table 2, Fig. 8). The orientation of the hypocenter patterns will be related to focal mechanism information to characterize the responsible structures.

5. Cluster focal mechanisms

So far, cluster analysis has been used for imaging seismogenic structures from relative locations of nearby earthquakes. In this section, we elaborate additional focal mechanisms from relocated clusters. This
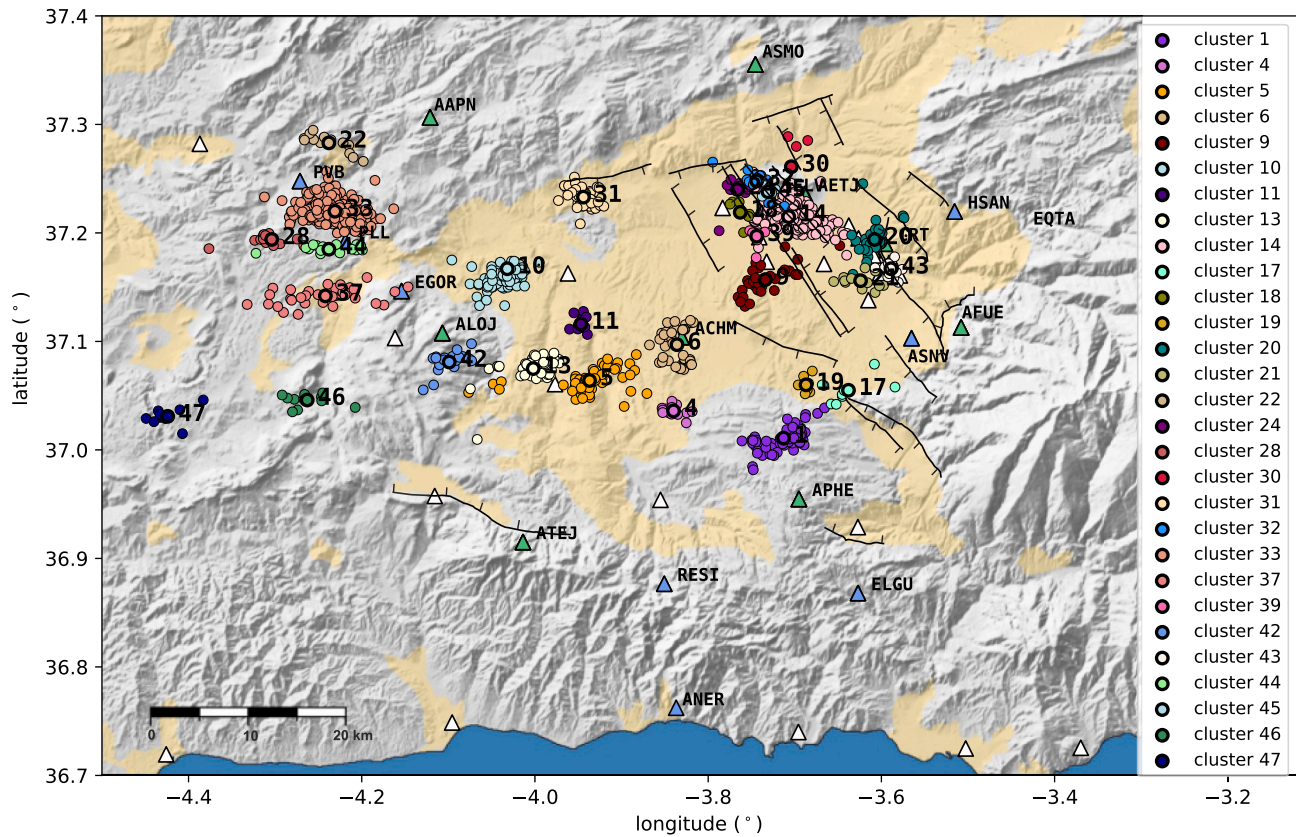
Fig. 6. Absolute locations of detected earthquake clusters (quarry blasts removed), colour coded according to legend. The centroid locations are given by circles with thick lines. Representations of faults and stations like Fig. 2.

is particularly relevant for clusters that cannot be connected to moment tensor solutions, and thus the kinematic description of these faulting sources is incomplete, lacking information on rake. For this purpose, we rely on classic focal mechanisms inversion from first motion polarities in vertical component seismogram. For clustered seismicity, we can stabilize first motion focal mechanisms substantially (Carmona et al., 2009). First, we obtain focal mechanisms from the set of composite first motion polarity measurements on the aligned waveforms of the cluster, which is typically larger and more accurate than polarity measurements for individual waveforms (Shearer et al., 2003). The different events are assumed to give redundant information, allowing to detect inappropriate polarity readings in presence of noise or technical problems of the instrumentation. The use of the mean hypocenter location from all multiple earthquakes reduces depth errors, stabilizing the estimation of take-off angles. Furthermore, we use the fault angle parameters from relative location as an a priori constraint in the search for first-motion focal-mechanisms, in order to restrict the model space and reduce ambiguity in cases where polarities alone are insufficient to constrain the nodal planes (Kilb and Hardebeck, 2006; Carmona et al., 2009).

We applied the analysis to the 23 relocated clusters with strike and dip angle estimates (Table 2). Stations with unclear or changing polarities are omitted. We obtain an average of 9 self-consistent polarity readings per cluster, which in their own are not sufficient for focal mechanism inversion for any of the clusters. To restrict the model space, we allow for faulting solutions with strike within 20° from the best-fitting plane from cluster relocation, leaving the dip and rake angles free. As an exception, for # 9 and 21 (dip of 11° y 7°, respectively) we constrain the dip value (from 0 to 30°), but do not restrict strike, to take into account the indetermination of strike for sub-horizontal planes. We perform grid search for suitable mechanisms using FOCMEC (Snoke, 2003), with angles determined from raytracing for the mean cluster location and the 1D Betic Earth model (see previous section). Since only

clear and consistent polarities are being used, polarity errors in the solution are not allowed. We were able to obtain focal mechanisms for 16 clusters (Fig. 9, Table 3). The solutions confirm the predominance of normal faulting mechanisms, in addition to a number of strike-slip sources, the latter concentrated west of the Granada Basin. Apart from being able to overcome a shortage of polarity readings, the composite cluster focal mechanisms are a complete kinematic description of the source, since the a priori knowledge of the cluster orientation allows resolving the nodal plane ambiguity inherent to point source mechanisms. In the following section, we compare cluster focal mechanisms to moment tensor solutions and assemble the seismotectonic model of the Granada Basin.

6. Discussion

6.1. Cross-validation of results

The combination of full waveform moment tensor inversion, cluster detection and relative location, and the inversion of cluster focal mechanisms allows for a comprehensive assessment of seismotectonic parameters in the Granada Basin, at least for structures that have shown activity in the last 35 years. The comparison of point source focal mechanisms and fault orientations from relocated seismicity allows overcoming the nodal plane ambiguity inherent to focal mechanisms on one hand, as well as the indetermination of slip vectors inherent to the structural interpretation of hypocenter alignments on the other hand. The different methodologies lead to overall consistent results, which is shown by the substantial agreement between the tendencies for focal depth, faulting style and fault orientation, as well as from the comparison of parameters for individual clusters and events. All three methodologies were applied to seismicity from the Iznajar-Loja and Santa Fe-Atarfe series (# 33 and 14). In the first case, three available moment
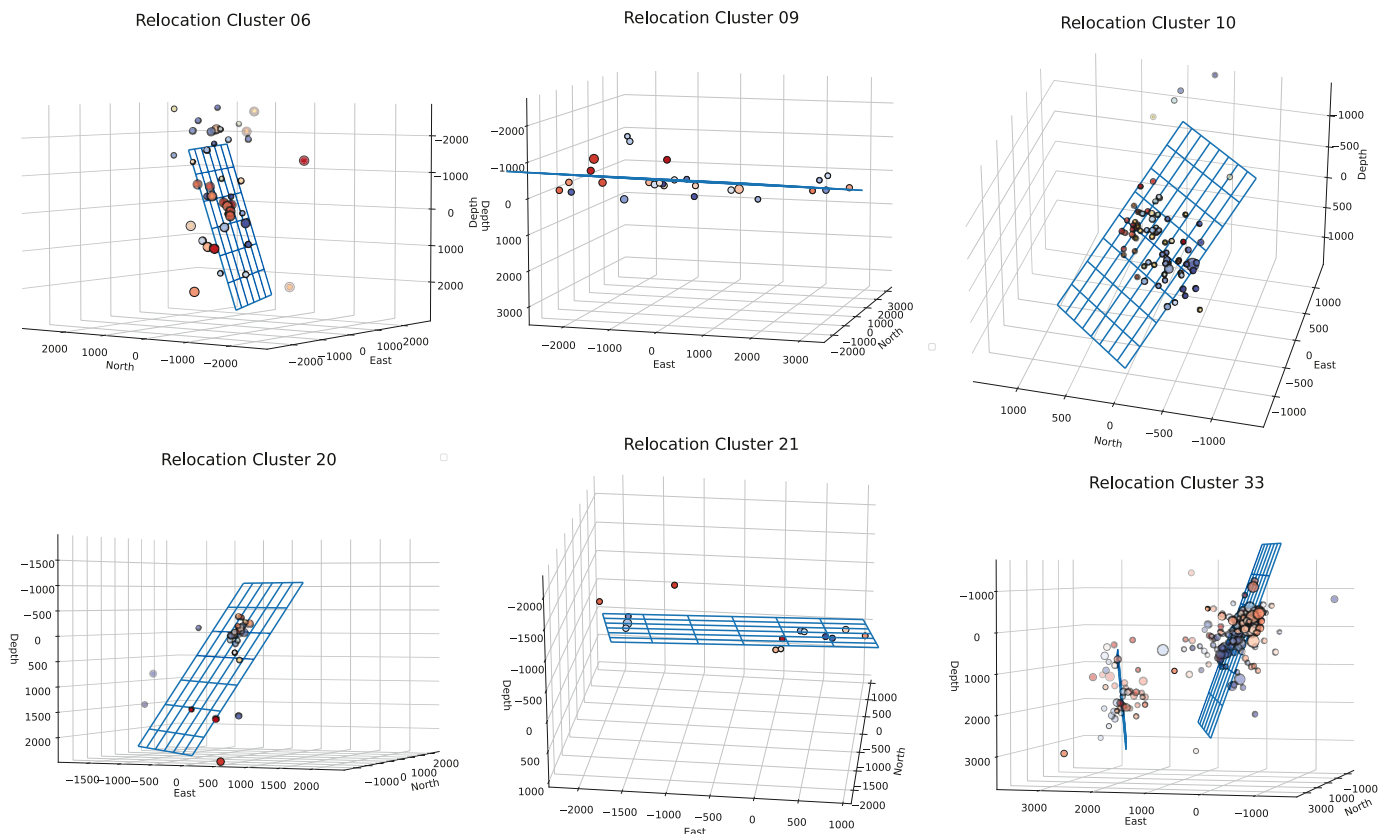
Fig. 7. Examples for relative locations in high-angle and low-angle clusters. All axes labeling in units [m], with master event at origin. Blue wireframe planes illustrate the cluster direction from principal component analysis. Hypocenters are represented with a diverging, blue (first events) to red (last events) colour map to illustrate migration of seismicity (# 10 and 33). (For interpretation of the references to colour in this figure legend, the reader is referred to the web version of this article.)

tensor solutions give average fault angles of strike N342°E, dip 58° and rake of −21°, compared to N343°E, dip 90° and rake of 0° for the cluster mechanism and strike N343°E, dip 74° for the best fitting plane. Centroid depths from 12 km to 14 km are similar to the cluster centroid location at 11.4 km depth. For the Santa Fe - Atarfe series, centroid depths of 5 km to 7 km and average source orientation from moment tensor inversion of strike N126°E, dip 41°, rake −106° compare favorably to cluster orientation of N124°E, dip 61°, cluster depth of 4.4 km and cluster mechanism of N100°E, dip 61°, and rake −102°.

Assuming planar geometry of faults, the discrepancies observed for the Iznajar-Loja and Santa Fe-Atarfe series are ≲ 30°, which, if characteristic for the rest of the dataset, allows a proper determination of faulting style and orientation. Larger deviations were observed only for cluster 10, near the locality of Salar, with moment tensor estimate of strike N284°E, dip 72° and rake −66°, and cluster orientation of N223°E with dip 56°. Even here both models agree on fairly steep fault dip in roughly NW direction, providing an acceptable qualitative description of this normal fault. The orientation of relocated clusters and cluster focal mechanism give similar results by construction, since the focal mechanisms grid search is limited to directions close to the best fitting plane. Nevertheless, we observe individual inconsistencies, for example for clusters 04 and 05, which show steep southward dip in relocation (78° and 71°, respectively), but steep northward dip in cluster mechanisms (80° and 81°, respectively). Strike directions agree within 3° and formal discrepancies are ≲ 30°, although this entails the reversal of fault dip polarity in this example, with significance for the tectonic characterization of the structures. A main source of uncertainty may be the predominance of short-period, vertical-component seismograms in relative location, implying that S-wave cross correlations may be contaminated by the P-wave coda and S to P conversions, and the

saturation of the signal at near stations for earthquakes ≳ magnitude 3. Within this limitation, we observe consistent source parameters within different areas of the Granada Basin, which are presented below.

6.2. Shallow structures in the NE-sector of the basin

A large share of seismicity corresponds to the northeastern sector of the Granada Basin, near Sierra Elvira and the Granada metropolitan area. In this section we include structures with centroid depths from 1 km to 9 km (# 14, 20, 24, 32, 39, 43, 45). The distributions of the relocated events show approximately NW-SE strike and dip to the SW (except for # 32). The cluster relocations suggest high-angle faulting, with dip angles from 60° to 74°. Several active normal faults in this sector have been recognized from surface geology (Sanz de Galdeano et al., 2003; Peláez et al., 2003; Galindo-Zaldívar et al., 2003; Madarieta-Txurruka et al., 2022; Lozano et al., 2022), and appear to be linked to recorded seismicity. We can compare cluster relocations to co-located moment tensors (20,070,104, 20,181,009, and Santa Fe-Atarfe series) and cluster focal mechanisms (# 14, 20, 24, 32, 39, 45) available for this group of earthquakes, confirming the normal faulting style. The only exception is # 39, showing the largest dip angle and strike-slip motion. For the normal faulting events, the average focal mechanism from moment tensor inversion is strike N125°E, dip 40°, rake −104°, and from cluster analysis N134°E, 60°, −92°, compared to an average cluster orientation of strike N132°E and dip 66°. Although these discrepancies may fall within the range of uncertainty (see previous section), at least in case of cluster 14 we may also suspect that they are produced by a listric geometry of the fault. Overall cluster dip (61°) is steeper than dip from moment tensor inversion (about 40°), while at the same time moment tensor centroids are deeper than the mean cluster location, suggesting

Table 2
Cluster assignment and relocation of detected multiplets in the Granada Basin. Columns; 1: Cluster number according to temporal order of the first events, 2: Number of members, 3–5: mean catalogue location as cluster centroid, 6: source type (earthquake or explosion), 7: geographical reference (not shown in map) and 8–9: Cluster orientation from Principal Component Analysis for hypocenter distributions with general planar shape. Strike values counted clockwise from north and dip positive to the right. For multiplet 33, two planes have been fitted to the western and eastern hypocenter clusters.

#	Events	Lon [°]	Lat [°]	Depth [km]	source	Near place:	Strike [°]	Dip [°]
1	70	−3.713	37.011	12.8	EQ	Venta del Fraile	N70E	64
2	21	−3.824	37.054	7.9	EXPL	Agrón	–	–
3	34	−3.633	37.280	13.7	EXPL	E Cubillas	–	–
4	19	−3.840	37.036	12.0	EQ	Agrón	N112E	75
5	66	−3.937	37.064	13.4	EQ	Cacín	N77E	71
6	39	−3.836	37.097	11.9	EQ	Ventas de Huelma	N68E	77
7	82	−4.158	37.137	4.4	EXPL	Sierra Gorda	–	–
8	27	−3.651	37.282	15.0	EXPL	E Cubillas	–	–
9	42	−3.734	37.157	9.7	EQ	S Santa Fe	N273E	11
10	107	−4.032	37.167	12.2	EQ	Salar	N223E	56
11	13	−3.947	37.116	11.7	EQ	Cacín	–	–
12	57	−4.358	37.090	2.2	EXPL	Sierra Gorda	–	–
13	54	−4.002	37.075	12.3	EQ	Santa Cruz del Comercio	–	–
14	563	−3.707	37.215	4.4	EQ	Santa Fe – Atarfe	N124E	61
15	24	−4.092	36.908	7.6	EXPL	Sierra Tejeda	–	–
16	176	−4.336	37.000	10.4	EXPL	SW Sierra Gorda	–	–
17	8	−3.638	37.055	12.5	EQ	El Puntal	–	–
18	10	−3.763	37.219	7.5	EQ	Fuente Vaqueros	–	–
19	8	−3.687	37.060	12.1	EQ	Suspiro del Moro	N131E	27
20	36	−3.608	37.194	6.8	EQ	Granada	N137E	62
21	17	−3.624	37.156	10.1	EQ	Armilla	N164E	7
22	14	−4.238	37.283	9.5	EQ	Iznájar	–	–
23	9	−4.152	37.134	4.3	EXPL	Sierra Gorda	–	–
24	17	−3.766	37.240	8.7	EQ	Pinos Puente	N113E	71
25	8	−4.098	36.905	6.7	EXPL	Sierra Tejeda	–	–
26	10	−3.626	37.292	17.3	EXPL	E Cubillas	–	–
27	42	−3.751	37.056	7.2	EXPL	Escúzar	–	–
28	18	−4.304	37.194	11.4	EQ	Villanueva de Tapia	N62E	77
29	20	−3.718	37.235	0.2	EXPL	Sierra Elvira	–	–
30	8	−3.704	37.261	6.3	EQ	S Cubillas	–	–
31	56	−3.944	37.233	14.9	EQ	Brácana	N244E	76
32	33	−3.744	37.248	3.8	EQ	Pinos Puente	N340E	71
33	325	−4.231	37.220	11.4	EQ	Iznájar- Loja, W- cluster:	N343E	74
						E- cluster:	N164E	86
34	69	−4.294	36.960	12.7	EXPL	SW Sierra Gorda	–	–
35	8	−3.565	36.935	11.9	EXPL	Valle de Lecrín	–	–
36	40	−3.577	36.938	10.8	EXPL	Valle de Lecrín	–	–
37	49	−4.242	37.142	10.9	EQ	Río Frío	N62E	73
38	22	−4.064	36.867	0.6	EXPL	Sierra Tejeda	–	–
39	12	−3.744	37.197	9.2	EQ	El Jau	N140E	74
40	76	−3.759	36.972	5.4	EXPL	Venta del Fraile	–	–
41	8	−3.752	36.991	5.0	EXPL	Venta del Fraile	–	–
42	19	−4.099	37.081	13.6	EQ	Sierra Gorda	N122E	88
43	19	−3.589	37.167	6.4	EQ	Zaidín	N128E	60
44	18	−4.238	37.185	14.6	EQ	Santa Barbara	N57E	81
45	25	−3.731	37.238	0.9	EQ	Pinos Puente	N130E	70
46	16	−4.263	37.046	14.4	EQ	W Sierra Gorda	N13E	70
47	9	−4.424	37.031	0.9	EQ	East Antequera	N134E	84

that the responsible fault may be progressively flattening out into the basal detachment.
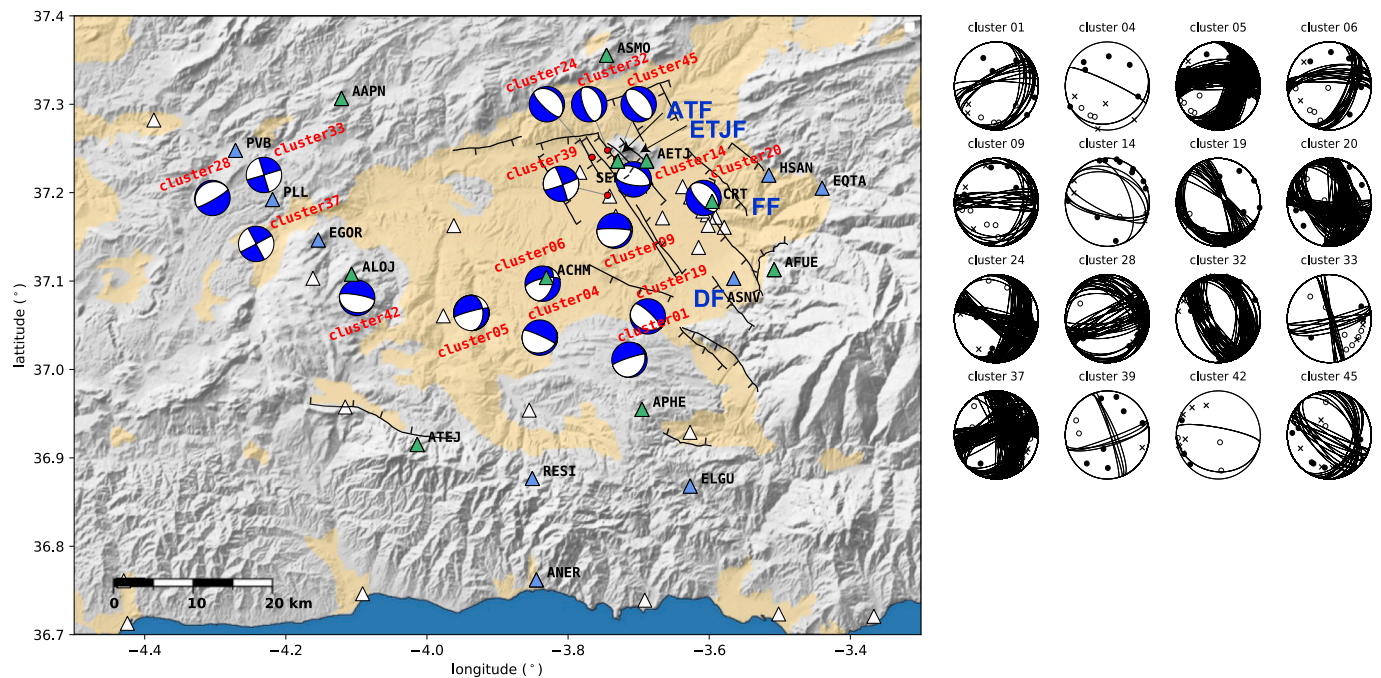
According to the absolute cluster locations, cluster orientations may be extrapolated to the surface, compared to fault traces and tentatively assigned to individual structures. # 20, composed mainly from events of the 1998 earthquake series beneath the city of Granada, with 6.8 km centroid depth, strike N137°E and dip angle of 62°, matches with the outcrop of the Fargue Fault (Fig. 8). A relationship between this series and the fault has been proposed previously (Sanz de Galdeano et al., 2012). Also, # 43, active in 2009, with cluster orientation of N128°E, 60° and located slightly south at 6.4 km depth, matches with the geometry of the Fargue Fault. # 45 near Sierra Elvira shows shallow depth of ~1 km and steep SW-ward dip of ~70°, which makes an extrapolation to the surface relatively straightforward. This cluster matches with the trace of the Atarfe Fault, sometimes referred to as Tajo Colorado Fault (Sanz de Galdeano et al., 2003; Madarieta-Txurruka et al., 2022), although taking into account the density of the fault network and realistic location accuracy, the cluster might possibly belong to the Pinos

Puente fault, as well. In a similar position we find # 14, associated with the 2021 Santa Fe-Atarfe series, which according to cluster and moment tensor depths is located deeper and probably behind the Atarfe Fault. We propose that this series involved the Ermita Tres Juanes fault as the most prominent mapped candidate structure in the footwall of the Atarfe fault (Azañón et al., 2012; Madarieta-Txurruka et al., 2022). # 32, containing events from the 2018 Pinos Puente seismic series, shows opposite dip direction. The cluster agrees with the steep dipping plane in moment tensor mechanism 20,181,009, at centroid depth of 3 km. We propose that this cluster activated a shallow antithetic fault in the hangingwall of the Pinos Puente fault, which could match with the Alitaje fault, visible in seismic sections (Sanz de Galdeano et al., 2003).

6.3. Mid-crustal structures in the southern sector

In the southern sector of the basin, we also find high-angle faults (# 1, 4, 5 and 6), although with notably different characteristics and orientation. Dip values from relocations range from 64° to 77°. The

Fig. 8. Location map of 23 clusters for which fault angle parameters were estimated. Black bars show the strike of the cluster. The lengths of the black bars represent the size of the clusters, with a minimum length of 1 km for the sake of visibility. The estimate of size is obtained for a circular fault area that contains the projections of 80% of the relocated events. Representations of faults and stations like Fig. 2. Faults discussed in the text are labeled in blue; ATF: Atarfe Fault, ETFJ: Ermita Tres Juanes Fault, DF: Dílar Fault, FF: El Fargue Fault. (For interpretation of the references to colour in this figure legend, the reader is referred to the web version of this article.)

strike of the structures scatters around an approximately *E*-W orientation, with values between N68°E and N112°E, representing a different trend compared to events in the northeast sector. The centroid locations of these clusters are systematically deeper, concentrating in a narrow depth interval from 12 to 13 km. This is matching with the sub-horizontal band of mid-crustal seismicity (Fig. 2) indicating that these clusters represent the activation of high-angle fault segments in vicinity of the basal detachment beneath the Granada Basin. A striking characteristic of the clusters is their continued activity over the monitoring period of 35 years (Fig. 5), a point we readdress in section 6.6. The size of the fault patches represented by # 1, 4, 5 and 6 is about 5 km, apparently confining seismicity between about 10 and 15 km depth, which is consistent with the width of the mid-crustal seismicity band from absolute locations. The orientation of the clusters show similarity to mapped faults, in particular the southward dipping La Malaha Fault (Azañón et al., 2007), but the extrapolation of fault patch geometries to the surface does not match with individual structures and the continuity and activity of the detected structures into the upper crust is unconstrained.

The approximately N-S of extension on the fault patches in this sector is consistent with available moment tensor solutions (events 19,981,118, 20,071,001, 20,091,105, 20,140,325, 20,170,518). The corresponding strike values range from N83°E to N107°E (with the possible exception of mechanism 19,981,118, where the E-W nodal plane shows a significantly shallower dip of 35°), comparable to strike values from cluster focal mechanisms, that range from N72°E to N114°E. The consistent values for strike directions are in contrast to controversial results for dip, where the cluster focal mechanisms suggest steep

northward dipping faults (compare section 6.1). According to our projection of first motion polarities, a southern fault dip is difficult to reconcile with normal faulting cinematics for these clusters. Here, cluster analysis is unable to discriminate between a *syn-* or antithetic arrangement of the fault segments near the detachment horizon, although moment tensor inversion suggests that both types of structures are involved, since southward (events 20,071,001 and 20,170,518) and northwards (events 20,091,105 and 20,140,325) fault dip directions can be observed for the steep-dipping nodal planes in this sector. The most prominent north dipping structure in the Granada Basin is the Zafarraya fault on the southern edge of the basin, but the mid-crustal clusters are at least 15 km apart from the fault trace and unrelated to this fault.

6.4. Low-angle structures in the central sector

Between these two groups of high-angle faults we find three clusters with notably different geometry, corresponding to low-angle hypocenter distributions (# 9, 19 and 21). Like the structures discussed in the previous section, also the low-angle clusters are characterized by long-lasting activity. They have depths between 10 and 12 km, again coincident with the prominent band of mid-crustal seismicity. The fundamental difference to the previous group of structures is the sub-horizontal orientation, with estimated dip of 7° and 11° for # 21 and 9. These clusters indicate that the sub-horizontal basal detachment beneath the basin itself is seismically active, apart from being a reference horizon for seismicity on nearby high-angle fault patches as seen in the previous section. # 19, with a NW-SE strike and dip of 27° to the SW, may be possibly associated with the deepest part of the Dílar fault, in

Fig. 9. a) Cluster focal mechanisms in lower hemisphere, equal area projection, labeled with the cluster number according to Table 2. For the sake of visibility, some mechanisms have been shifted from the cluster locations (gray lines). Representation of relief, sediments, faults and seismic stations like in Fig. 2. Green and blue stations, used for cluster analysis and relocations, also provide the largest part of polarity readings. b) Focal mechanism grid search for individual clusters. Filled and open circles represent the projections of compressive and dilatational polarity readings, respectively. (For interpretation of the references to colour in this figure legend, the reader is referred to the web version of this article.)

Table 3

Cluster focal mechanisms. Cluster number, centroid location and geographical reference as in Table 2. Mechanism given through the active nodal plane, with strike values counted clockwise from north and dip positive to the right.

#	Lon [°]	Lat [°]	Depth [km]	Near place:	Strike [°]	Dip [°]	Rake [°]
1	−3.713	37.011	12.8	Venta del Fraile	N252E	80	−80
4	−3.840	37.036	12.0	Agrón	N294E	80	−80
5	−3.937	37.064	13.4	Cacín	N254E	81	−60
6	−3.836	37.097	11.9	Ventas de Huelma	N256E	64	−56
9	−3.734	37.157	9.7	S Santa Fe	N45E	14	−145
14	−3.707	37.215	4.4	Santa Fe – Atarfe	N99E	61	−102
19	−3.687	37.060	12.1	Suspiro del Moro	N105E	22	−117
20	−3.608	37.194	6.8	Granada	N137E	60	−90
24	−3.766	37.240	8.7	Pinos Puente	N134E	70	−90
28	−4.304	37.194	11.4	Villanueva de Tapia	N60E	80	−90
32	−3.744	37.248	3.8	Pinos Puente	N330E	40	−90
33	−4.231	37.220	11.4	Iznájar- Loja	N343E	90	0
37	−4.242	37.142	10.9	Río Frío	N332E	90	0
39	−3.744	37.197	9.2	El Jau	N340E	84	−8
42	−4.099	37.081	13.6	Sierra Gorda	N280E	75	−90
45	−3.731	37.238	0.9	Pinos Puente	N141E	50	−90

accordance with a listric geometry of the fault systems in the eastern part of the basin as they approach the detachment horizon. The location of # 9 coincides with moment tensor solution 19,961,228, with depth 12 km and one low-angle nodal plane (30°). Other moment tensor mechanisms possibly associated with the basal detachment are 19,970,224, 20,030,910 and 20,170,629, with nodal plane dip of 4°,17° and 31°, respectively, although the assignment of the mechanisms is uncertain in each individual case, since their position, depths and orientations are also similar to the steep dipping segments of the southern

sector (see previous section). Nevertheless, the fault kinematics can be confirmed from cluster focal mechanism for # 9 and 19, with dip of 14° and 22° respectively.

The average slip vector from the available mechanisms indicates direction of transport of the hanging wall block towards SSW (mean azimuth N211°E), providing a key parameter for understanding the present-day tectonics of the Granada Basin. The SSW transport direction is sub-parallel to the principal extensional strain axes of many mechanisms in the southern sector of the basin, while it is significantly rotated from the downdip direction of the NW-SE striking faults that border the basin to the east, and also from the overall Betic WSW extension from GNSS observations. The clusters confirm seismic activity of the basal detachment of the basin, although limited to small fault patches with diameters close to 3 km. The three clusters span an area of about 100 km^2, which gives a lower bound for the size of the detachment surface in the brittle crust. This does not imply that the detachment is to be considered a seismogenic structure. Creeping low-angle normal faults may exist above the brittle-ductile transition, and there is a general lack of moderate-to-large earthquakes on such structures in the seismological record (e.g., Collettini, 2011). To shed more light on this issue, we will examine the temporal pattern of detachment-related seismicity in section 6.6.

6.5. Structures in the western sector

Near the western limit of the Granada Basin, we observed the presence of clusters with relatively small dimensions and variable orientations, mostly located at depths between 11 and 15 km. The clusters are characterized by low magnitudes (m ≤ 3), except for # 10 and 33, with maximum magnitudes M$_W$ 3.5 (Table 1). These are also the two most relevant clusters in terms of dimension (600 m and 1 km, respectively) and number of events (> 100). # 10 is related to activity near Salar in September and October 2022, and related to normal faulting (moment tensor 20,220,929), with strike N223°E and dip of 56°. The distribution of hypocenters for # 33, containing the Iznájar-Loja seismic series,

reveals geometric complexity, showing two separate fault segments (compare section 4). Strike (N343°E and N164°E) and dip values (74° and 86°) are in agreement with strike-slip mechanisms obtained for this series (moment tensors 19980413 A,B, 19980414). The strike-slip kinematics and ~ N-S orientation inferred for the Iznájar-Loja series coincides with a previous analysis of multiplets using high-frequency waveforms (Carmona et al., 2009) and with fault plane measurements (Reicherter and Peters, 2005). Strike-slip faulting could represent a regional trend, since similarly oriented mechanisms were involved for example in the 1951, M_w 5.2 and M_w 5.3 Jaén earthquakes, ~30 km north of the Granada Basin (Batlló et al., 2008). At the eastern limit of the area, the orientation and normal faulting cinematics of # 42 appear similar to the structural elements in the southern Basin (section 6.3), and the transition between the two domains cannot be defined precisely.

6.6. Temporal characteristics of earthquake activity

We already established that part of the seismicity in the Granada Basin occurs in the form of seismic series, with a pronounced burst of activity over a short period of time (e.g., Saccorotti et al., 2002; Carmona et al., 2009). Often these series lack a prominent main shock, as

was the case of the Iznajar-Loja series (# 33), with three earthquakes of moment magnitude Mw 3.5 to 3.6, or the Santa Fe-Atarfe series (# 14), with five earthquakes between Mw 4.1 and 4.4. On the other hand, many detected clusters contain events from different years (Fig. 3), indicating sustained seismic activity on the responsible structures. To examine the significance of these two end members of cluster activity, we represent the normalized cumulative event count within clusters, organized according to the four groups of structures discussed in sections 6.2 to 6.5 (Fig. 10). Event production rate is showing a dichotomous nature, and can be divided into two fundamentally different subsets. Clusters in the western sector and clusters representing high-angle faults in the northeastern sector show a pronounced step-like history of event production, illustrating the occurrence of sequences concentrated in time. In case of series from the northeastern sector, the temporal concentration appears somewhat less pronounced than for the western basin, including series in which activity is resumed several times over the observation period. The two remaining groups show a fundamentally different temporal pattern, with continuous activity at similar event production rate over practically the entire 35-year duration of local seismic network operation. Short-lasting clusters sometimes show a unidirectional component of hypocenter migration along the fault plane in the course of the swarm
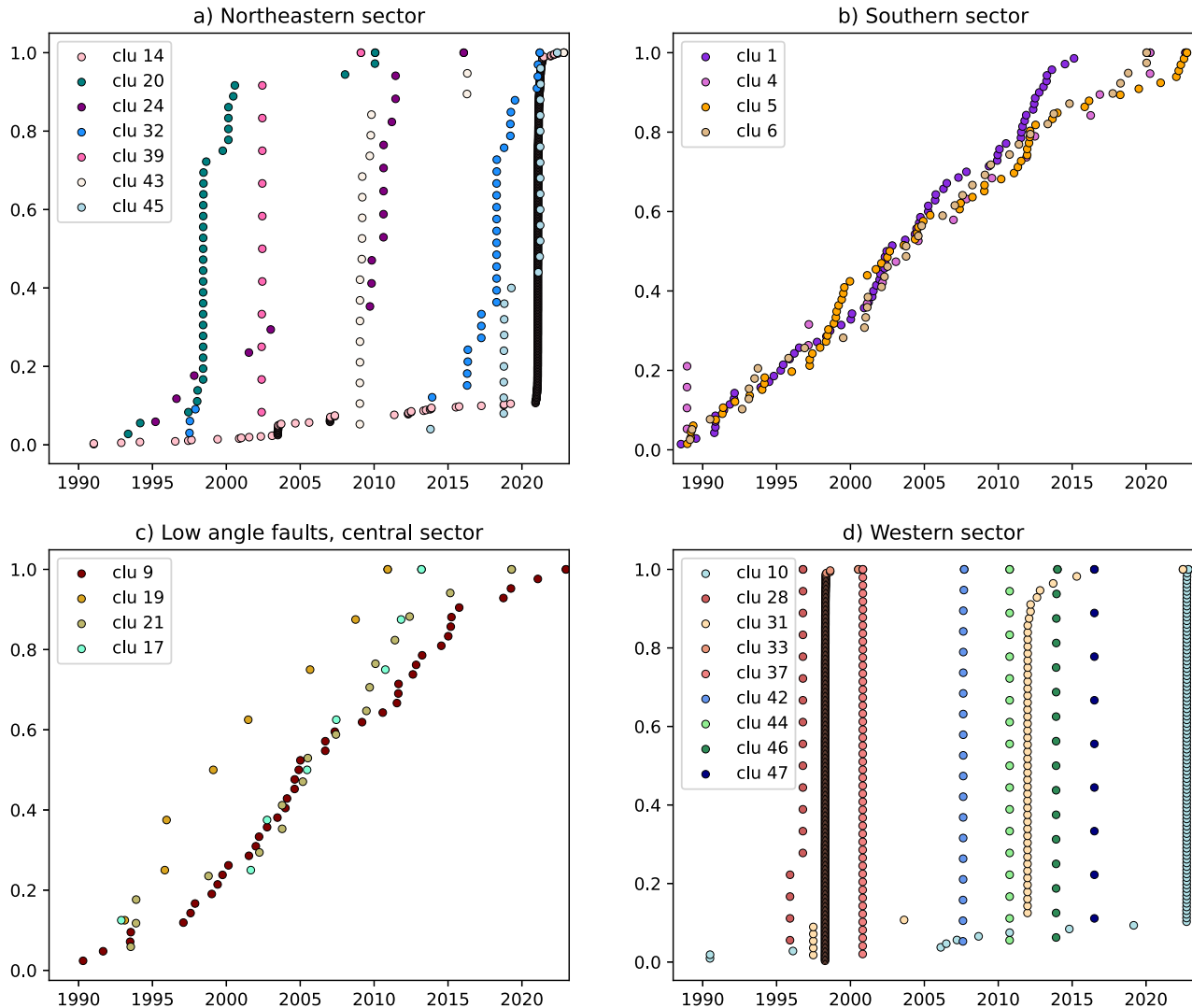
Fig. 10. Normalized cumulative event count in clusters versus time (years 1988–2022), sorted by groups of structures (as sections 6.2–6.5). The curves illustrate the stepwise histories of event production for clusters in groups 1 and 4, versus a steady event production rate for clusters in groups 2 and 3 related to the mid-crustal detachment.

(Fig. 7), which has not been observed for the long-lasting clusters.

Long-lasting activity is observed for the mid-crustal structures in the southern sector and the low-angle structures in the central sector, both in the vicinity of the basal detachment beneath the Granada Basin. A stable event production rate for clusters located on different points along the detachment horizon suggests that the low-angle normal fault at the base of the basin releases stress continuously and over a broad area, loading the individual patches of the low-angle structure (group 3) or nearby faults (group 2) at a relatively constant rate. Such a seismological expression of detachment creep resembles the situation in the Corinth Rift (Rigo et al., 1996; Hatzfeld et al., 2000), Aegean Sea (Toker, 2021) or the Apennines (Michele et al., 2020; Waldhauser et al., 2021), where earthquake clusters mark the position and extend of coupled fault patches, representing elastic asperities along the creeping low-angle faults (Anderlini et al., 2016), as well as synthetic and antithetic normal faults in the hanging wall block of the detachment (Chiaraluce et al., 2007). Low-angle normal faulting is expected to occur on structures with low frictional strength, generally promoting aseismic slip or creep (Collettini, 2011). Within an overall picture of continuity of the detachment-related clusters, we can perceive a second-order change in the last quarter of the monitoring period: The average event production rate in the clusters of groups 2 and 3 is approximately constant during 26 years from the start of the local earthquake catalogue in 1988 to end of 2013, but appreciably lower during the 9 years from 2014 to 2022 (Figs. 10, 11). It is unclear if these changes in event production rate can be related to variations of aseismic slip (Vuan et al., 2020), but it is remarkable that the decrease is mainly driven by # 1, 19 and 17, which are located in the same area and may reflect an actual change of the local situation.

6.7. Seismotectonic model for the Granada Basin

Our results show the distribution of different faulting trends in the Granada Basin and illustrate their relationship. On a NE-SW trending transect across the basin we can track the succession of shallow high angle normal faulting on the NE-side, the activity of coupled fault patches along the detachment horizon in the central basin, and mid-crustal, high-angle fault patches in the southern sector where the main detachment surface is becoming deeper (Fig. 11). We can relate several seismic series to mapped active faults in the northeastern sector of the Basin, which match with the dip and location of relocated clusters and related focal mechanisms. In particular, we find evidence for seismic activity on the Fargue fault (# 20 and 43), Ermita Tres Juanes Fault (# 14), Atarfe fault (# 45), as well as the Alitaje Fault as example for an active antithetic structure (# 32). Besides high fault dip angles near 60° for shallow clusters, there are available some estimates for intermediate fault dip between ~25° and ~ 45°, for example from moment tensors for the 2021 Santa Fe-Atarfe series (Ermita Tres Juanes Fault) or cluster 17, presumably located near the base of the Dílar fault, which suggests that the high angle normal faults may be flattening out as the approach the detachment horizon. The listric geometry may induce hanging-wall rollover, explaining the presence of basement highs in the footwalls of synthetic normal faults inside the Granada Basin (e.g. Sierra Elvira, and La Malaha fault, Azañón et al., 2007).

The high angle normal faults connect at depth with a SW-wards dipping layer of concentrated seismicity between 10 and 15 km (Fig. 11). From the appearance of long-term sequences with.

steady event production rate for clusters in this volume we infer that the basal detachment is moving aseismically (Chiaraluce et al., 2007; Anderlini et al., 2016; Toker, 2021). Also the spatial distribution of seismicity is more continuous along the detachment horizon, compared to the shallow crust, which reinforces our impression of a dichotomous nature of the seismicity in the basin. The SW limit of a localized and seismologically detectable detachment seems to coincide with the brittle-ductile transition at 14–15 km depth (Fig. 11), below which rocks become too ductile to build up elastic strain. Aseismic creep of the basal detachment is driving continuous seismicity on the embedded asperities (low-angle clusters) and the adjoining portion of other faults (high-angle clusters). Microseismic surveys along creeping or presumably creeping faults for example in the Apennines (Michele et al., 2020, Waldhauser
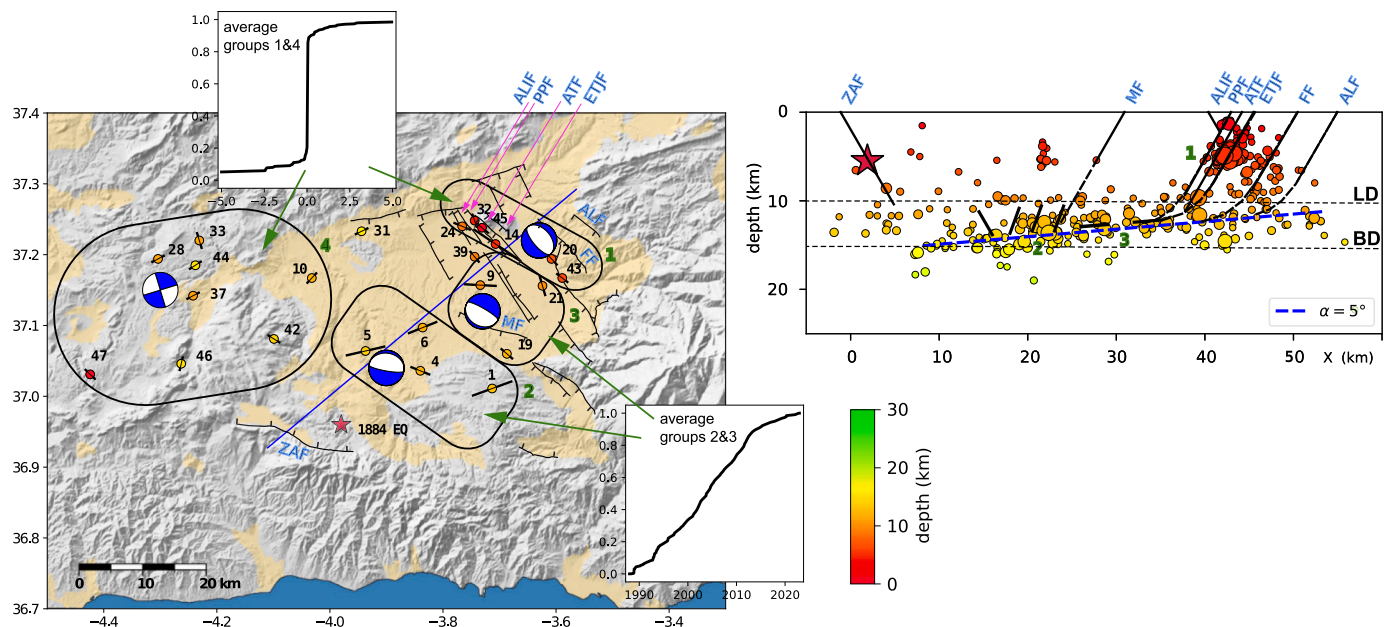
Fig. 11. Cluster strike directions (black bars, compare Fig. 8) and representative focal mechanisms for the four different seismogenic domains discussed in sections 6.2 to 6.5. Representations of faults and stations like Fig. 2. The inlays illustrate the dichotomous nature of event production rate in discrete clusters (top) and continuous clusters related to aseismic creep of the basal detachment (bottom, compare Fig. 10). Right side: Seismotectonic section showing the projection of catalogue seismicity (M ≥ 2.8, 4.15°W-3.45°W, 36.75°N-38.35°N), detected clusters and faults from surface geology in NE-SW direction (blue line in map). Faults discussed in the text are labeled in blue (ALIF: Alitaje Fault, PPF: Pinos Puente Fault, ATF: Atarfe Fault, ETFJ: Ermita Tres Juanes Fault, ALF: Alfacar Fault, FF: El Fargue Fault, MF: La Malahá fault, ZAF: Ventas de Zafarraya Fault). (For interpretation of the references to colour in this figure legend, the reader is referred to the web version of this article.)

et al., 2021), the Calabrian arc (Brozzetti et al., 2017; Cirillo et al., 2022) or the Corinth Rift zone (Rigo et al., 1996; Hatzfeld et al., 2000; Lambotte et al., 2014) show an analogous arrangement of low angle and high angle structures in the mid-crustal shear zone. Geodetic evidence for aseismic creep on low-angle normal faults (Hreinsdóttir and Bennett, 2009; Anderlini et al., 2016) suggests that the upper limit of microseismicity marks the locking depth of the faults. In case of the Granada Basin this suggests a locking depth of 10 km, permitting an estimate for the downdip width of seismic ruptures on high-angle normal faults. Shallow structures above the locking depth move in sporadic earthquakes or seismic series with step-like histories of cumulative event counts, separated by long periods of seismic quiescence, in accordance with the low deformation rate of the basin.

Current seismicity data cannot provide support for an extension of the basal detachment beyond the limits of the Granada Basin. In particular, the seismological defined detachment appears to be located deeper than the Mecina detachment, a low-angle basement fault outcropping about 5 km distance from the high-angle faults (Martínez-Martínez, 2006), and which has been considered as a candidate structure for the master fault beneath the Granada Basin (Galindo-Zaldívar et al., 1996; Madarieta-Txurruka et al., 2021). A regional-scale extension of the detachment towards the Guadix-Baza Basin (Martin-Rojas et al., 2023) may be consistent with the geometry of mid-crustal seismicity in the Granada Basin, although the barrier of high topography and current lack of earthquakes between the two basins does not provide further evidence for such a configuration. On the other hand, fault displacement along the detachment may be transferred to the surface through the high-angle normal faults at the eastern border of the basin, as the seismotectonic section indicates continuity and interaction between both types of structures (Fig. 11). The presence of ~2 km of sediments in several depocentres in the basin (Morales et al., 1990, Rodríguez-Fernández and Sanz de Galdeano, 2006), as well as the important activity of the mountain front inferred from river entrenchment and geomorphology (Pérez-Peña et al., 2010) point to a significant combined fault throw at the NW-SE normal faulting structures. This suggests that the boundary faults at the eastern edge of the Granada Basin have transferred a significant amount of extension from the basal detachment to the surface. Clusters west of the basin take place at the depth of the detachment horizon, however showing different faulting style and orientation (with the exception of # 42), and impulsive histories of event production, which suggests that the detachment does not extend into this sector either.

We recall that the identification and characterization of seismogenic elements from instrumental seismicity for the period 1988–2022 may show only a subset of the existing structures. Notably, no individual clusters or events over the last 35 years could have been assigned to several of the major faults with clear morphological expression and evidence for associated paleoearthquakes. This includes the Ventas de Zafarraya Fault (Reicherter et al., 2003), the Malahá Fault (Azañón et al., 2007), the Granada Fault (Azañón et al., 2009) as well as possibly the Padul-Niguelas Fault (Alfaro et al., 2001), although the seismogenic nature of this later fault has been questioned explicitly (Gil et al., 2017; Abad et al., 2022). The Padul-Niguelas Fault and the Malahá Fault are candidate structure to explain archaeoseismological evidence for a M6 event in the 13th century CE (Forlin et al., 2024). In particular, the Ventas de Zafarraya Fault can be considered a verified seismogenic structure, as in addition to inferred paleoearthquakes with recurrence times of about 2 ka (Grützner et al., 2013), there is available historical and geological evidence for rupture during the 1884 earthquake. For our observation period, starting 103 years after the last significant event, the crustal volume around the Ventas de Zafarraya Fault is characterized by a virtual absence of seismicity. By analogy, we should not take the lack of instrumental seismicity on other active Quaternary faults in the Granada basin as indication of aseismic behavior.

7. Conclusions

Despite the solid evidence for large earthquakes in the Granada basin happening in historical times, the instrumental seismicity recorded since the start of the local network in 1988 is limited to low magnitudes. Individual seismogenic elements of the Granada Basin have been identified and characterized using three different techniques. Moment tensor inversion from regional three-component waveforms was applied to the most energetic events (M_W 3.4 to 5.0). 32 moment tensor solutions for the Granada Basin show a predominance of normal faulting, consistent with the extensional tectonic environment. The vast majority of events are located in the upper crust at depths shallower than 15 km. We further classify events with similar waveforms over 35 years into clusters, to image active structures through relative location. After the removal of quarry blasts, with characteristic source time distributions during working hours, we were able to estimate the position and orientation of 23 fault patches. Relative locations reveal shallow (1–9 km), NW-SE-trending structures associated with surface faults only in the northeastern sector of the basin. The seismically active structures in the southern sector are high-angle ~E-W-trending fault patches between 10 km and 15 km depth, which we identify with a basal detachment beneath the basin. The sub-horizontal detachment can be directly visualized over an area of ~100 km^2 through the presence of event clusters with low-angle fault dip. Finally, 16 additional focal mechanisms have been obtained by combining composite first motion polarity measurements within clusters with the fault orientations from relative location. Available source mechanisms suggest a ~ SSW ward transport direction of the basal detachment, compared to a general ~WSW motion of the Western Betics with respect to stable Iberia according to GNSS data.

Observed seismicity clusters show very different temporal behavior, including discrete seismic series with fast moment release, as well as continuous earthquake clusters with steady event production rate over the entire observation period. The latter clusters can be associated with the basal detachment and are a byproduct of aseismic creep, where displacement along the detachment accumulates gradually. High-angle and low-angle fault systems in the Granada Basin interact with each other, as shown by the continuous seismic activity on high-angle structures near the detachment horizon. There is currently no seismological evidence for an extend of the basal detachment beneath the limits of the basin, which instead might interact with the listric normal faults to transfer displacement to the surface on the northeastern side of the basin. The brittle-ductile transition appears to limit the seismologically detected detachment on the southwestern side. The upward limit of the mid-crustal seismicity band at ~10 km may represent the locking depth for major structures and the downdip limit of large ruptures at high-angle normal faults. Several shallow clusters and focal mechanisms match with recognized fault structures, providing support for a seismogenic behavior of the Fargue, Ermita Tres Juanes, Atarfe, and Alitaje faults. The inventory of seismogenic structures developed in this study is intrinsically incomplete due to the limited time span covered by local seismic instrumentation, which may be a relevant limitation in view of the slow deformation and long recurrence intervals in the study area. For new seismic series arising and small-to-moderate earthquakes at the Granada Basin, we now dispose of a modern, dense recording network that permits routine applications of modern seismological analysis tools.

CRediT authorship contribution statement

Daniel Stich: Writing – original draft, Methodology, Investigation, Funding acquisition, Formal analysis, Conceptualization. **Jose Morales:** Writing – review & editing, Methodology, Investigation, Formal analysis. **José Ángel López-Comino:** Writing – review & editing, Investigation, Funding acquisition, Formal analysis. **Carlos Araque-Pérez:** Writing – review & editing, Investigation, Formal analysis. **José Miguel Azañón:** Writing – review & editing, Investigation. **Miguel Ángel**

Dengra: Writing – review & editing, Investigation, Formal analysis. **Mario Ruiz:** Writing – review & editing, Investigation. **Moisés Weber:** Writing – review & editing, Investigation, Funding acquisition.

Declaration of competing interest

The authors declare that they have no known competing financial interests or personal relationships that could have appeared to influence the work reported in this paper.

Data availability

The sources of earthquake hypocenter parameters, geological maps, GNSS velocities, Quaternary fault parameters and previous moment tensor solutions are references in the figure captions. Additional numerical data about cluster assignment, absolute and relative locations are available in a repository (Stich, 2024).

References

Abad, I., Nieto, F., Reolid, M., Jiménez-Millán, J., 2022. Evidence of phyllosilicate alteration processes and clay mineral neoformation promoted by hydrothermal fluids in the Padul Fault area (Betic Cordillera, SE Spain). Appl. Clay Sci. 230, 106669.

Alfaro, P., Galindo-Zaldívar, J., Jabaloy, A., López-Garrido, A.C., Sanz de Galdeano, C., 2001. Evidence for the activity and paleoseismicity of the Padul fault (Betic Cordillera, southern Spain). Acta Geol. Hisp. 36, 283–295.

Alguacil, G., 1986. Los instrumentos de una Red Sísmica telemétrica para microterremotos. La Red Sísmica de la Universidad de Granada. Ph.D. Thesis. University of Granada, p. 232.

Alguacil, G., Guirao, J.M., Gómez, F., Vidal, F., De Miguel, F., 1990. Red Sísmica de Andalucía (RSA): a digital PC-Based seismic network. Cah. Cent. Europ. Géodyn. Séismol. 1, 19–27.

Anderlini, L., Serpelloni, E., Belardinelli, M.E., 2016. Creep and locking of a low-angle normal fault: Insights from the Altotiberina fault in the Northern Apennines (Italy). Geophys. Res. Lett. 43, 4321–4329. https://doi.org/10.1002/2016GL068604.

Azañón, J.M., Booth-Rea, G., Martínez-Martínez, J.M., Pérez-Peña, V., 2007. Actividad tectónica durante la época medieval y romana en la cuenca de Granada (la falla de La Malaha). Resúmenes XII Reunión Nacional de Cuaternario, Ávila, p. 131.

Azañón, J.M., García-Mayordomo, J., Insua-Arévalo, J.M., Rodríguez-Peces, M.J., 2009. Palaeoseismological features of the Granada fault. In: 1st IQUA-IGCP 567 International Workshop on Earthquake Archaeology and Paleoseismology. Baelo Claudia, Cádiz, Spain.

Azañón, J.M., Pérez-Peña, J.V., Giaconia, F., Booth-Rea, G., Martínez-Martínez, J.M., Rodríguez-Peces, M.J., 2012. Active tectonics in the central and eastern Betic Cordillera through morphotectonic analysis: the case of Sierra Nevada and Sierra Alhamilla. J. Iber. Geol. 38 (225–238), 225.

Basili, R., Kastelic, V., Demircioglu, M.B., Garcia Moreno, D., Nemser, E.S., Petricca, P., Sboras, S.P., Besana-Ostman, G.M., Cabral, J., Camelbeeck, T., Caputo, R., Danciu, L., Domac, H., Fonseca, J., García-Mayordomo, J., Giardini, D., Glavatovic, B., Gulen, L., Ince, Y., Pavlides, S., Sesetyan, K., Tarabusi, G., Tiberti, M., Utkucu, M., Valensise, G., Vanneste, K., Vilanova, S., Wössner, J., 2013. The European Database of Seismogenic Faults (EDSF) Compiled in the Framework of the Project SHARE. https://doi.org/10.6092/INGV.IT-SHARE-EDSF.

Basili, R., Danciu, L., Beauval, C., Sesetyan, K., Vilanova, S., Adamia, S., Arroucau, P., Atanackov, J., Baize, S., Canora, C., Caputo, R., Carafa, M., Cushing, M., Custódio, S., Demircioglu Tumsa, M., Duarte, J., Ganas, A., García-Mayordomo, J., Gómez de la Peña, L., Gràcia, E., Jamšek Rupnik, P., Jomard, H., Kastelic, V., Maesano, F., Martín-Banda, R., Martínez-Loriente, S., Neres, M., Perea, H., Sket-Motnikar, B., Tiberti, M., Tsereteli, N., Tsironi, V., Vallone, R., Vanneste, K., Zupančič, P., 2022. European Fault-Source Model 2020 (EFSM20): online data on fault geometry and activity parameters. Istit. Nazion. Geof. Vulcanol. (INGV). https://doi.org/10.13127/efsm20.

Batlló, J., Stich, D., Palombo, B., Macia, R., Morales, J., 2008. The 1951 M_w 5.2 and M_w 5.3 Jaén, Southern Spain, Earthquake Doublet Revisited. Bull. Seismol. Soc. Am. 98, 1535–1545. https://doi.org/10.1785/0120070038.

Bezada, M.J., Humphreys, E.D., 2012. Contrasting rupture processes during the April 11, 2010 deep-focus earthquake beneath Granada, Spain. Earth Planet. Sci. Lett. 353, 38–46.

Bezada, M.J., Humphreys, E.D., Toomey, D.R., Harnafi, M., Dávila, J.M., Gallart, J., 2013. Evidence for slab rollback in westernmost Mediterranean from improved upper mantle imaging. Earth Planet. Sci. Lett. 368, 51–60.

Biggs, J., Bergman, E., Emmerson, B., Funning, G.J., Jackson, J., Parsons, B., Wright, T.J., 2006. Fault identification for buried strike-slip earthquakes using InSAR: the 1994 and 2004 Al Hoceima, Morocco earthquakes. Geophys. J. Int. 166, 1347–1362.

Brozzetti, F., Cirillo, D., Liberi, F., Piluso, E., Faraca, E., De Nardis, R., Lavecchia, G., 2017. Structural style of Quaternary extension in the Crati Valley (Calabrian Arc): evidence in support of an east-dipping detachment fault. Ital. J. Geosci. 136 (3), 434–453. https://doi.org/10.3301/IJG.2017.11.

Buforn, E., Udías, A., Madariaga, R., 2011. Intermediate and deep earthquakes in Spain. Pure. Appl. Geophys. 136, 375–393. https://doi.org/10.1007/BF00878576.

Capella, W., Spakman, W., van Hinsbergen, D.J.J., Chertova, M.V., Krijgsman, W., 2020. Mantle resistance against Gibraltar slab dragging as a key cause of the Messinian Salinity Crisis. Terra Nova 32, 141–150. https://doi.org/10.1111/ter.12442.

Carmona, E., Stich, D., Ibáñez, J.M., Saccorotti, G., 2009. Multiplet Focal Mechanisms from Polarities and Relative Locations: the Iznajar Swarm in Southern Spain. Bull. Seismol. Soc. Am. 99, 3421–3429. https://doi.org/10.1785/0120090036.

Cesca, S., Şen, A.T., Dahm, T., 2014. Seismicity monitoring by cluster analysis of moment tensors. Geophys. J. Int. 196 (3), 1813–1826.

Chiaraluce, L., Chiarabba, C., Collettini, C., Piccinini, D., Cocco, M., 2007. Architecture and mechanics of an active low-angle normal fault: Alto Tiberina Fault, northern Apennines, Italy. J. Geophys. Res. 112, B10310. https://doi.org/10.1029/2007JB005015.

Chung, W.Y., Kanamori, H., 1976. Source process and tectonic implications of the Spanish deep-focus earthquake of March 29, 1954. Phys. Earth Planet. Inter. 13, 85–96. https://doi.org/10.1016/0031-9201(76)90073-X.

Cirillo, D., Totaro, C., Lavecchia, G., Orecchio, B., de Nardis, R., Presti, D., Ferrarini, F., Bello, S., Brozzetti, F., 2022. Structural complexities and tectonic barriers controlling recent seismic activity in the Pollino area (Calabria–Lucania, southern Italy) – constraints from stress inversion and 3D fault model building. Solid Earth 13, 205–228. https://doi.org/10.5194/se-13-205-2022.

Collettini, C., 2011. The mechanical paradox of low-angle normal faults: current understanding and open questions. Tectonophysics 510, 253–268. https://doi.org/10.1016/j.tecto.2011.07.015.

Danciu, L., Sesetyan, K., Demircioglu, M., Gülen, L., Zare, M., Basili, R., Elias, A., Adamia, S., Tsereteli, N., Yalçin, H., Utkucu, M., Khan, M.A., Sayab, M., Hessami, K., Rovida, A.N., Stucchi, M., Burg, J.P., Karakhanian, A., Babayan, H., Avanesyan, M., Mammadli, T., Al-Qaryouti, M., Kalafat, D., Varazanashvili, O., Erdik, M., Giardini, D., 2018. The 2014 earthquake model of the middle east: Seismogenic sources. Bull. Earthq. Eng. 16 (8), 3465–3496.

Espinar-Moreno, M., 2022. Estudio de la documentación de los terremotos granadinos de 1431. In: Estudios sobre Patrimonio. Cultura y Ciencias Medievales, 24, Anexo. Granada. ISSN: e-2341-3549.

Ester, M., Kriegel, H., Sander, J., Xu, X., 1996. A Density-based Algorithm for Discovering Clusters in large Spatial Databases with Noise. In: Proceedings of 2nd International Conference on Knowledge Discovery and Data Mining (KDD-96), pp. 226–231.

Faccenna, C., Piromallo, C., Crespo-Blanc, A., Jolivet, L., Rossetti, F., 2004. Lateral slab deformation and the origin of the western Mediterranean arcs. Tectonics 23. https://doi.org/10.1029/2002TC001488.

Fichtner, A., Villaseñor, A., 2015. Crust and upper mantle of the western Mediterranean – Constraints from full-waveform inversion. Earth Planet. Sci. Lett. 428, 52–62.

Forlin, P., Reicherter, K., Gerrard, C.M., Bailiff, I., García Porras, A., 2024. Recovering a lost seismic disaster. The destruction of El Castillejo and the discovery of the earliest historic earthquake affecting the Granada region (Spain). PLoS One 19 (4), e0300549. https://doi.org/10.1371/journal.pone.0300549.

Galindo-Zaldívar, J., Jabaloy, A., González-Lodeiro, F., 1996. Reaction of the Mecina detachment in the Western sector of Sierra Nevada (Betic Cordilleras, SE Spain). C. R. Acad. Sci. 323 (7), 615–622.

Galindo-Zaldívar, J., Jabaloy, A., Serrano, I., Morales, J., González-Lodeiro, F., Torcal, F., 1999. Recent and present-day stresses in the Granada Basin (Betic Cordilleras): example of a late Miocene-present-day extensional basin in a convergent plate boundary. Tectonics 18, 686–702. https://doi.org/10.1029/1999TC900016.

Galindo-Zaldívar, J., Gil, A.J., Borque, M.J., González-Lodeiro, F., Jabaloy, A., Marín-Lechado, C., Ruano, P., Sanz de Galdeano, C., 2003. Active faulting in the internal zones of the central Betic Cordilleras (SE, Spain). J. Geodyn. 36, 239–250. https://doi.org/10.1016/S0264-3707(03)00049-8.

Garate, J., Martin-Davila, J., Khazaradze, G., Echeverria, A., Asensio, E., Gil, A.J., de Lacy, M.C., Armenteros, J.A., Ruiz, A.M., Gallastegui, J., Alvarez-Lobato, F., Ayala, C., Rodríguez-Caderot, G., Galindo-Zaldívar, J., Rimi, A., Harnafi, M., 2015. Topo-Iberia project: CGPS crustal velocity field in the Iberian Peninsula and Morocco. GPS Solutions 19, 287–295. https://doi.org/10.1007/s10291-014-0387-3.

García-Mayordomo, J., Martín-Banda, R., . Guide for the use of QAFI v.4. http://info.igme.es/qafi/. Instituto Geológico y Minero de España (IGME), CSIC, Madrid, Spain. https://doi.org/10.13140/RG.2.2.12873.01121.

García-Mayordomo, J., Insua-Arévalo, J., Martínez-Díaz, J., Jiménez-Díaz, A., Martín-Banda, R., Álvarez-Gómez, J., Rodríguez-Peces, M., Pérez-López, R., Rodríguez-Pascua, M., Masana, E., Perea, H., Martín-González, F., Giner-Robles, J., Nemser, E., Cabral, J., Compilers Q, 2012. The Quaternary Active Faults Database of Iberia (QAFI v.2.0). J. Iber. Geol. 38 (1), 285–302. https://doi.org/10.5209/rev_JIGE.2012.v38.n1.39219.

Gil, A.J., Galindo-Zaldívar, J., Sanz de Galdeano, C., Borque, M.J., Sánchez-Alzola, A., Martínez-Martos, M., Alfaro, P., 2017. The Padul normal fault activity constrained by GPS data: Brittle extension orthogonal to folding in the central Betic Cordillera. Tectonophysics 712-713, 64–71.

Grützner, C., Ruano, P., Jabaloy, A., Galindo-Zaldívar, J., Becker-Heidmann, P., Sanz de Galdeano, C., Rudersdorf, A., Reicherter, K., 2013. Late Holocene rupture history of the Ventas de Zafarraya Fault (Southern Spain). Cuatern. Geomorfol. 27 (3–4), 5–32.

Gutscher, M.-A., Dominguez, S., Westbrook, G.K., Le Roy, P., Rosas, F., Duarte, J.C., Terrinha, P., Miranda, J.M., Graindorge, D., Gailler, A., Sallares, V., Bartolome, R., 2012. The Gibraltar subduction: a decade of new geophysical data. Tectonophysics 574, 72–91.

Hanks, T.C., Kanamori, H., 1979. A moment magnitude scale. J. Geophys. Res. 84, 2348–2350.

Hatzfeld, D., Karakostas, V., Ziazia, M., Kassaras, I., Papadimitriou, E., Makropoulos, K., Voulgaris, N., Papaioannou, C., 2000. Microseismicity and faulting geometry in the Gulf of Corinth (Greece). Geophys. J. Int. 141, 438–456.

Heimann, S., Kriegerowski, M., Isken, M., Cesca, S., Daout, S., Grigoli, F., Juretzek, C., Megies, T., Nooshiri, N., Steinberg, A., Sudhaus, H., Vasyura-Bathke, H., Willey, T., Dahm, T., 2017. Pyrocko - an Open-Source Seismology Toolbox and Library. V. 0.3. GFZ Data Services. https://doi.org/10.5880/GFZ.2.1.2017.001.

Heit, B., Mancilla, F., Yuan, X., Morales, J., Stich, D., Martín, R., Molina-Aguilera, A., 2017. Tearing of the mantle lithosphere along the intermediate-depth seismicity zone beneath the Gibraltar Arc: the onset of lithospheric delamination. Geophys. Res. Lett. 44, 4027–4035. https://doi.org/10.1002/2017GL073358.

Hreinsdóttir, S., Bennett, R., 2009. Active aseismic creep on the Alto Tiberina low-angle normal fault, Italy. Geology 37, 683–686. https://doi.org/10.1130/G30194A.1.

Instituto Geográfico Nacional, 2020. CartoBase ANE (cartografía base del Atlas Nacional de España, atlasnacional.ign.es/wane/Geología).

International Seismological Centre, 2023. On-line Bulletin. https://doi.org/10.31905/D808B830.

Kilb, D., Hardebeck, J.L., 2006. Fault parameter constraints using relocated earthquakes: a validation of first-motion focal-mechanism data. Bull. Seismol. Soc. Am. 96, 1140–1158.

Konstantaras, A.J., Katsifarakis, E., Maravelakis, E., Skounakis, E., Kokkinos, E., Karapidakis, E., 2012. Intelligent spatial-clustering of seismicity in the vicinity of the Hellenic Seismic Arc. Earth Sci. Res. 1, 1–10.

Kreemer, C., Blewitt, G., Klein, E.C., 2014. A geodetic plate motion and Global Strain Rate Model. Geochem. Geophys. Geosyst. 15, 3849–3889. https://doi.org/10.1002/2014GC005407.

Lambotte, S., Lyon-Caen, H., Bernard, P., Deschamps, A., Patau, G., Nercessian, A., Pacchiani, F., Bourouis, S., Drilleau, M., Adamova, P., 2014. Reassessment of the rifting process in the western Corinth Rift from relocated seismicity. Geophys. J. Int. 197 (3), 1822–1844.

Lonergan, L., White, N., 1997. Origin of the Betic-Rif mountain belt. Tectonics 16, 504–522.

López-Comino, J.A., Mancilla, F., Morales, J., Stich, D., 2012. Rupture directivity of the 2011, Mw 5.2 Lorca earthquake (Spain). Geophys. Res. Lett. 39, L03301 https://doi.org/10.1029/2011GL050498.

Lozano, L., Cantavella, J.V., Gaite, B., Ruiz-Barajas, S., Antón, R., Barco, J., 2022. Seismic analysis of the 2020–2021 Santa Fe seismic sequence in the Granada Basin, Spain: relocations and Focal Mechanisms. Seismol. Res. Lett. 93 (6), 3246–3265. https://doi.org/10.1785/0220220097.

Madarieta-Txurruka, A., Galindo-Zaldívar, J., González-Castillo, L., Peláez, J.A., Ruiz-Armenteros, A.M., Henares, J., Garrido-Carretero, M.S., Avilés, M., Gil, A.J., 2021. High- and Low-Angle Normal Fault activity in a Collisional Orogen: the Northeastern Granada Basin (Betic Cordillera). Tectonics 40 (7), n/a. https://doi.org/10.1029/2021TC006715.

Madarieta-Txurruka, A., González-Castillo, L., Peláez, J.A., Ruano, P., Catalán, M., Henares, J., Gil, A.J., Lamas-Fernández, F., Galindo-Zaldívar, J., 2022. The Role of Faults as Barriers in Confined Seismic Sequences: 2021 Seismicity in the Granada Basin (Betic Cordillera). Tectonics 41 (9), n/a. https://doi.org/10.1029/2022TC007481.

Mancilla, F., Del Pezzo, E., Stich, D., Morales, J., Ibañez, J.M., Bianco, F., 2012. QP and QS in the upper mantle beneath the Iberian Peninsula from recordings of the very deep Granada earthquake of April 11, 2010. Geophys. Res. Lett. 39, L09303.

Mancilla, F., Stich, D., Berrocoso, M., Martín, R., Morales, J., Fernández-Ros, A., Páez, R., Pérez-Peña, A., 2013. Delamination in the Betic Range; deep structure, seismicity, and GPS motion. Geology 41 (3), 307–310. https://doi.org/10.1130/G33733.1.

Mancilla, F., Booth-Rea, G., Stich, D., Pérez-Peña, J.V., Morales, J., Azañon, J.M., Martin, R., Giacomia, F., 2015. Slab rupture and delamination under the Betics and Rif constrained from receiver functions. Tectonophysics 663, 225–237.

Martín, R., Stich, D., Morales, J., Mancilla, F., 2015. Moment tensor solutions for the Iberian-Maghreb region during the Iberarray deployment. Tectonophysics 663, 261–274.

Martínez-Martínez, J.M., 2006. Lateral interaction between metamorphic core complexes and less-extended, tilt-block domains: the Alpujarras strike-slip transfer fault zone (Betics, SE Spain). J. Struct. Geol. 28, 602–620. https://doi.org/10.1016/j.jsg.2006.01.012.

Martin-Rojas, I., Alfaro, P., Galindo-Zaldivar, J., Borque-Arancón, M.J., García-Tortosa, F.J., Sanz de Galdeano, C., Avilés, M., Sánchez-Alzola, A., González-Castillo, L., Ruano, P., Medina-Cascales, P.I., Tendero-Salmerón, V., Madarieta-Txurruka, A., Pedrosa-González, M.T., Gil-Cruz, A.J., 2023. Insights of active extension within a collisional orogen from GNSS (Central Betic Cordillera, S Spain). Tectonics 42, e2022TC007723. https://doi.org/10.1029/2022TC007723.

Maurer, H., Deichmann, N., 1995. Microearthquake cluster detection based on waveform similarities, with an application to the western Swiss Alps. Geophys. J. Int. 123, 588–600.

Mezcua, J., Martínez Solares, J.M., 1983. Sismicidad del área Ibero-Mogrebí. Publicación 203. Instituto Geográfico Nacional, Madrid, p. 301.

Michele, M., Chiaraluce, L., Di Stefano, R., Waldhauser, F., 2020. Fine-scale structure of the 2016–2017 Central Italy seismic sequence from data recorded at the Italian National Network. J. Geophys. Res. Solid Earth 125, e2019JB018440. https://doi.org/10.1029/2019JB018440.

Mohadjer, S., Ehlers, T.A., Bendick, R., Stübner, K., Strube, T., 2016. A Quaternary fault database for Central Asia. Nat. Hazards Earth Syst. Sci. 16, 529–542. https://doi.org/10.5194/nhess-16-529-2016.

Morales, J., Vidal, F., De Miguel, F., Alguacil, G., Posadas, A.M., Ibáñez, J.M., Guzmán, A., Guirao, J.M., 1990. Basement structure of the Granada basin, Betic Cordilleras, southern Spain. Tectonophysics 177 (4), 337–348. https://doi.org/10.1016/0040-1951(90)90394-N.

Morales, J., Singh, S.K., Ordaz, M., 1996. Analysis of the Granada (Spain) earthquake of 24 June, 1984 (M = 5) with emphasis on seismic hazard in the Granada Basin. Tectonophysics 257, 253–263.

Morales, J., Serrano, I., Vidal, F., Torcal, F., 1997. The depth of the earthquake activity in the Central Betics (Southern Spain). Geophys. Res. Lett. 24 (24), 3289–3292. https://doi.org/10.1029/97GL03306.

Palano, M., González, P.J., Fernández, J., 2015. The Diffuse Plate boundary of Nubia and Iberia in the Western Mediterranean: crustal deformation evidence for viscous coupling and fragmented lithosphere. Earth Plant. Sci. Lett. 430, 439–447. https://doi.org/10.1016/j.epsl.2015.08.040.

Peláez, J.A., Sanz de Galdeano, C., López Casado, C., 2003. Use of active fault data versus seismicity data in the evaluation of seismic hazard in the Granada Basin (Southern Spain). Bull. Seismol. Soc. Am. 93, 1670–1678.

Pérez-Peña, J.V., Azor, A., Azañón, J.M., Keller, E.A., 2010. Active tectonics in the Sierra Nevada (Betic Cordillera, SE Spain): insights from geomorphic indexes and drainage pattern analysis. Geomorphology 119, 74–87.

Pérez-Peña, J.V., Azañón, J.M., Azor, A., Booth-Rea, G., Galve, J.P., Roldán, F.J., Mancilla, F., Giaconia, F., Morales, J., Al-Awabdeh, M., 2015. Quaternary landscape evolution driven by slab-pull mechanisms in the Granada Basin (Central Betics). Tectonophysics 663, 5–18. https://doi.org/10.1016/j.tecto.2015.07.035.

Petersen, G.M., Niemz, P., Cesca, S., Mouslopoulou, V., Bocchini, G.M., 2021. Clusty, the waveform-based network similarity clustering toolbox: concept and application to image complex faulting offshore Zakynthos (Greece). Geophys. J. Int. 224, 2044–2059. https://doi.org/10.1093/gji/ggaa568.

Randall, G.E., 1994. Efficient calculation of complete differential seismograms for laterally homogeneous earth models. Geophys. J. Int. 118, 245–254.

Reicherter, K.R., Peters, G., 2005. Neotectonic evolution of the Central Betic Cordilleras (southern Spain). Tectonophysics 405, 191–212.

Reicherter, K.R., Jabaloy, A., Galindo-Zaldívar, J., Ruano, P., Becker- Heimann, P., Morales, J., Reiss, S., González-Lodeiro, F., 2003. Repeated palaeoseismic activity of the Ventas de Zafarraya fault (S Spain) and its relation with the 1884 Andalusian earthquake. Int. J. Earth Sci. 92, 912–922. https://doi.org/10.1007/s00531-003-0366-3.

Rigo, A., Lyon-Caen, H., Armijo, R., Deschamps, A., Hatzfeld, D., Makropoulos, K., Papadimitriou, P., Kassaras, I., 1996. A microseismic study in the western part of the Gulf of Corinth (Greece): implications for largescale normal faulting mechanisms. Geophys. J. Int. 126, 663–688.

Rodríguez-Fernández, J., Azor, A., Azañón, J.M., 2011. The betic intramontane basins (SE Spain): stratigraphy, subsidence, and tectonic history. In: Busby, C., Azor, A. (Eds.), Tectonics of Sedimentary Basins. https://doi.org/10.1002/9781444347166.ch23.

Rodríguez-Fernández, J.C., Sanz de Galdeano, C., 2006. Late orogenic intramontane basin development: the Granada Basin, Betics (southern Spain). Basin Res. 18, 85–102. https://doi.org/10.1111/j.1365- 2117.2006.00284.x.

Saccorotti, G., Carmona, E., Ibáñez, J.M., Del Pezzo, E., 2002. Spatial characterization of Agrón, southern Spain, 1988–1989 seismic series. Phys. Earth Planet. Inter. 129, 13–29.

Santos-Bueno, N., Fernandez-Garcia, C., Stich, D., Mancilla, F., Martin, R., Molina-Aguilera, A., Morales, J., 2019. Focal mechanisms for subcrustal earthquakes beneath the Gibraltar Arc. Geophys. Res. Lett. 46 (5), 2534–2543.

Sanz de Galdeano, C., Peláez, J.A., López Casado, C., 2003. Seismic potential of the main active faults in the Granada Basin (southern Spain). Pure Appl. Geophys. 160, 1537–1556. https://doi.org/10.1007/s00024-003-2359-3.

Sanz de Galdeano, C., García-Tortosa, F.J., Peláez, J.A., Alfaro, P., Azañón, J.M., Galindo- Zaldívar, J., López-Casado, C., López-Garrido, A.C., Rodríguez-Fernández, J., Ruano, P., 2012. Main active faults in the Granada and Guadix-Baza Basins (Betic Cordillera). J. Iber. Geol. 38, 209–223.

Serpelloni, E., Vannucci, G., Pondrelli, S., Argnani, A., Casula, G., Anzidei, M., Baldi, P., Gasperini, P., 2007. Kinematics of the Western Africa-Eurasia Plate Boundary From Focal Mechanisms and GPS Data. Geophys. J. Int. 25 https://doi.org/10.1111/j.1365-246X.2007.03367.x.

Serpelloni, E., Cavaliere, A., Martelli, L., Pintori, F., Anderlini, L., Borghi, A., Randazzo, D., Bruni, S., Devoti, R., Perfetti, P., Cacciaguerra, S., 2022. Surface Velocities and Strain-Rates in the Euro-Mediterranean Region From Massive GPS Data Processing. Front. Earth Sci. 10, 907897 https://doi.org/10.3389/feart.2022.907897.

Shearer, P.M., Hardebeck, J.L., Astiz, L., Richards-Dinger, K.B., 2003. Analysis of similar event clusters in aftershocks of the 1994 Northridge, California, earthquake. J. Geophys. Res. 108 https://doi.org/10.1029/2001JB000685.

Silver, P.G., Jordan, T.H., 1982. Optimal estimation of scalar seismic moment. Geophys. J. R. Astron. Soc. 70, 755–787.

Skoumal, R.J., Kaven, J.O., Walter, J.I., 2019. Characterizing seismogenic fault structures in Oklahoma using a relocated template-matched Catalogue. Seismol. Res. Lett. 90, 1535–1543. https://doi.org/10.1785/0220190045.

Snoke, J., 2003. 85.12 FOCMEC: FOCal MEChanism determinations. Intern. Geophys. 81, 1629–1630. https://doi.org/10.1016/S0074-6142(03)80291-7.

Spakman, W., Chertova, M.V., van den Berg, A., van Hinsbergen, D.J.J., 2018. Puzzling features of western Mediterranean tectonics explained by slab dragging. Nat. Geosci. 11, 211–216. https://doi.org/10.1038/s41561-018-0066-z.

Stich, D., 2024. Earthquake clustering in the Granada Basin (doi:10.7910/DVN/MGCK49, Harvard Dataverse, V1).

Stich, D., Alguacíl, G., Morales, J., 2001. The relative location of multiplets in the vicinity of the Western-Almería (southern Spain) earthquake series of 1993–94. Geophys. J. Int. 146, 801–812.

Stich, D., Ammon, C.J., Morales, J., 2003. Moment tensor solutions for small and moderate earthquakes in the Ibero-Maghreb region. J. Geophys. Res. 108, 2148.

Stich, D., Mancilla, F., Baumont, D., Morales, J., 2005. Source analysis of the Mw 6.32004 Al Hoceima earthquake (Morocco) using regional apparent source time functions. J. Geophys. Res. 110, B06306 https://doi.org/10.1029/2004JB003366.

Stich, D., Serpelloni, E., Mancilla, F., Morales, J., 2006. Kinematics of the Iberia–Maghreb plate contact from seismic moment tensors and GPS observations. Tectonophysics 426 (3), 295–317. https://doi.org/10.1016/j.tecto.2006.08.004.

Stich, D., Martín, R., Morales, J., 2010. Moment tensor inversion for Iberia-Maghreb earthquakes 2005–2008. Tectonophysics 48, 390–398.

Stich, D., Martínez-Solares, J.M., Custódio, S., Batlló, J., Martín, R., Teves-Costa, P., Morales, J., 2020. Seismicity of the Iberian Peninsula. In: Quesada, C., Oliveira, J.T. (Eds.), The Geology of Iberia: A Geodynamic Approach. Regional Geology Reviews. https://doi.org/10.1007/978-3-030-10,931-8-311.

Styron, R., Pagani, M., 2020. The GEM global active faults database. Earthquake Spectra 36 (1_suppl), 160–180. https://doi.org/10.1177/8755293020944182.

Styron, R., García-Pelaez, J., Pagani, M., 2020. CCAF-DB: the Caribbean and Central American active fault database. Nat. Hazards Earth Syst. Sci. 20, 831–857. https://doi.org/10.5194/nhess-20-831-2020.

Toker, M., 2021. Symptomatic discretization of small earthquake clusters reveals seismic coupling to 2017 Bodrum earthquake (Mw 6.6) in the Gulf of Gokova (SW corner of Turkey): viscous-compliant seismogenesis over back-arc setting. J. Afr. Earth Sc. 177, 104156.

Vidal, F., 1986. Sismotectónica de la Región Béticas-Mar de Alborán. Ph.D. Thesis. University of Granada.

Vidal, F., 2011. El terremoto de Alhama de Granada de 1884 y su impacto. Anuari Verdaguer 11–45.

Vidale, J.E., Shearer, P.M., 2006. A survey of 71 earthquake bursts across southern California: exploring the role of pore fluid pressure fluctuations and aseismic slip as drivers. J. Geophys. Res. 111, B05312 https://doi.org/10.1029/2005JB004034.

Vuan, A., Brondi, P., Sugan, M., Chiaraluce, L., Di Stefano, R., Michele, M., 2020. Intermittent Slip Along the Alto Tiberina Low-Angle Normal Fault in Central Italy. Geophys. Res. Lett. 47 https://doi.org/10.1029/2020GL089039.

Waldhauser, F., 2001. HypoDD-A program to compute double-difference hypocenter locations, U.S. Geol. Surv. 1–25 (Open-File Rept. 01–113).

Waldhauser, F., Ellsworth, W.L., 2000. A double-difference earthquake location algorithm: method and application to the northern Hayward fault. Bull. Seismol. Soc. Am. 90, 1353–1368.

Waldhauser, F., Michele, M., Chiaraluce, L., Di Stefano, R., Schaff, D.P., 2021. Fault planes, fault zone structure and detachment fragmentation resolved with high precision aftershock locations of the 2016–2017 central Italy sequence. Geophys. Res. Lett. 48 https://doi.org/10.1029/2021GL092918.